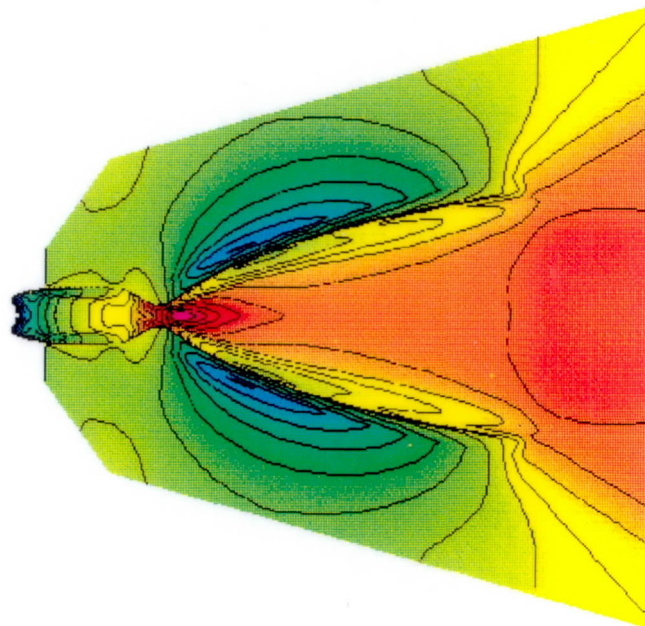# CFD Research Corporation

**CFDRC**

3325-D Triana Blvd., Huntsville, AL 35805, (205) 536-6576 FAX: (205) 536-6590

# COMPUTATIONAL ANALYSIS

# OF VARIABLE THRUST ENGINE (VTE)

# PERFORMANCE

## Final Report



by

## M.G. Giridharan, A. Krishnan, and A.J. Przekwas
### CFD Research Corporation
### 3325 Triana Blvd.
### Huntsville, AL 35805

# CFD Research Corporation

**CFDRC**

## COMPUTATIONAL ANALYSIS OF VARIABLE THRUST ENGINE (VTE) PERFORMANCE

**Final Report**

By

M.G. Giridharan, A. Krishnan, and A.J. Przekwas
CFD Research Corporation
3325 Triana Blvd.
Huntsville, AL 35805

February 1993

CFDRC Report 4075/3

For

National Aeronautic and Space Administration
George C. Marshall Space Flight Center
Huntsville, AL 35812

R&D Services and Software for Computational Fluid Dynamics (CFD)

# PREFACE

This is a final report summarizing the work performed under Phase III (third year) of a three phase (three year) research study entitled, "Orbital Maneuvering Vehicle (OMV) Thrust Chamber Performance". The study has been performed by CFD Research Corporation under NASA MSFC Contract: NAS8-37196. Mr. Klaus Gross of the EP55 branch, Propulsion Lab, was the project monitor.

The authors wish to acknowledge the technical guidance of Mr. Klaus Gross of MSFC and Dr. Ashok Singhal of CFD Research Corporation. The authors also wish to acknowledge the support of TRW, Inc., in providing the VTE engine geometry details and some test data. The guidance of Dr. R. Avva of CFD Research Corporation in implementing the radiation model is appreciated. The effort of Ms. J.L. Swann in preparing this document is also appreciated.

4075/3

**PROJECT SUMMARY**

This is the final report documenting the progress made during Phase III of a 3 year program to develop a comprehensive modeling methodology for evaluating the performance of the Variable Thrust Engine (VTE). Interim reports have been delivered at the end of Phases I and II.

Design and development of liquid rocket engines is currently based on overall performance characteristics at design operating conditions. The VTE is expected to operate over a range of power levels (from 10% to 100%) without sacrificing much efficiency/performance. The design of such engines requires a good understanding of the interactions between various complex physical phenomena such as atomization, spray dynamics, vaporization, convective/radiative heat transfer, turbulent mixing, and chemical reactions. The objective of this study was to develop and incorporate models for the above phenomena into an existing CFD code to facilitate detailed simulations of the VTE. The major highlights of this study are:

1.  The development of a non-orthogonal, body-fitted coordinate (BFC) model to reproduce the geometry of the thrust chamber/nozzle, the pintle, and the heat shield.

2.  The development and incorporation of a 2-liquid, two-phase, Eulerian-Lagrangian spray model into the CFD code. The spray model is fully coupled with the gas model. The droplet sizes are estimated from a linear surface wave model for impinging jets.

3.  The development of a chemical equilibrium model to simulate the hypergolic reaction between MMH and NTO. Thirteen species were considered in this model. The equilibrium chemistry model can also be used for other propellant combinations such as Hydrogen and Oxygen. An instantaneous reaction model and a finite-rate chemistry model are also available in the code.

4. The development of a discrete-ordinate radiation model to predict the effects of radiative heat transfer on the performance of the VTE and study of the effects of radiation heat shield.

5. A series of simulations were performed to estimate the effects of drop sizes, spray dynamics, chemistry, radiative heat transfer, on the VTE performance.

6. The simulations were performed at three different power levels namely 10%, 50%, and 100%.

The results indicate that the use of a gas-gas model to analyze the VTE implies an inappropriate approximation and the computed flow field is not realistic. It is necessary to use a 2-liquid spray model to simulate the droplet dynamics in the chamber. The simulations show that smaller droplets result in faster evaporation and better mixing, leading to improved engine performance. Larger droplets penetrate deep into the flow and impinge on the splash plate giving rise to an uneven vaporization distribution. The use of a chemical equilibrium model was necessary to bring predictions in better agreement with the data. Simplified finite rate models are unable to account for the generation and production of a number of species encountered in the VTE chamber. The results also indicate that radiative heat transfer is a small fraction of the convective/conductive heat transfer within the VTE and at the chamber/nozzle wall.

This report presents detailed descriptions of the models, simulations, and discusses the scope of desirable future work.

# TABLE OF CONTENTS

**TABLE OF CONTENTS (Continued)**

# LIST OF ILLUSTRATIONS

**LIST OF ILLUSTRATIONS (Continued)**

# LIST OF ILLUSTRATIONS (Continued)

Page

4075/3

# LIST OF ILLUSTRATIONS (Continued)

Page

4075/3

## NOMENCLATURE

### Section 3.1

| | |
|---|---|
| $\mu_j$ | chemical potential |
| $\mu_j{}^o$ | standard state Gibbs function |
| $p_j$ | partial pressure of species 'j' |
| $a_{ij}$ | number of atoms in 'i' and 'j' |
| $R$ | universal gas constant |
| $n_j$ | number of moles of species 'j' |
| $c_j$ | molar concentration of species 'j' |

### Section 3.2

| | |
|---|---|
| $\Omega$ | direction of propagation of radiation beam |
| $I$ | radiation beam intensity |
| $k$ | absorption coefficient of the gas medium |
| $\sigma$ | scattering coefficient of the gas medium |
| $\phi$ | phase function for gas scattering |
| $\varepsilon$ | wall emissivity |
| $\rho$ | wall reflectivity |
| $\mu, \xi, \eta$ | direction cosines of the radiation beam in x, y, r, directions |
| $\omega_m$ | weighting function for the mth ordinate |
| $I_b$ | black body radiation |
| $x', y'$ | local grid coordinates |
| $J$ | Jacobian of coordinate transformation |
| $F$ | grid transformation vectors |
| $\delta$ | angular redistribution function |
| $\forall$ | volume of the computational cell |
| $\alpha$ | weighting function for the numerical scheme |

Section 3.3

$m_d$     mass of the droplet

v       droplet velocity

U       gas velocity

$A_d$     droplet surface area

$V_d$     volume of the droplet

$g$       gravity vector

$C_D$     droplet drag coefficient

Re     Reynolds number

Sh     Sherwood number

$d$       diameter of the droplet

$D$       mass diffusion coefficient

$x_v, x_\alpha$   vapor mass fraction at droplet surface and free stream

Sc     Schmidt number

$C_d$     specific heat of the droplet

$T_d, T_g$   droplet and gas temperatures

$\dot{q}$       sensible heat transferred to droplet

$k$       thermal conductivity of the gas

Nu     Nusselt number

Pr     Prandtl number

$h_v$     enthalpy of vaporization of the droplet

$y_k$     mass fraction of species 'k'

Section 3.4

$\sigma$       standard deviation of turbulence probability distribution function

$k$       turbulent kinetic energy

$t_e$      turbulent eddy lifetime

$t_r$      eddy transit time

$\ell_e$      eddy characteristic length scale

$\tau$       droplet relaxation time

## Section 3.5

$H$      thickness of the liquid sheet

$\omega$      growth rate of the instability wave

$\sigma$      surface tension

$k$      wavenumber of the instability wave

## Abbreviations

| | |
|---|---|
| MMH | MonoMethyl Hyradazine |
| NTO | Nitrogen Tetra-oxide |
| OMV | Orbital Maneuvering Vehicle |
| VTE | Variable Thrust Engine |
| BFC | Body Fitted Coordinate |
| SMD | Sauter Mean Diameter |
| PISO | Pressure Implicit Split Operator |
| SIMPLE | Semi-Implicit Method for Pressure-Linked Equations |
| MUSCL | Monotonic Upwind Scheme for Conservation Law |
| TDK | Two-Dimensional Kinetics |

4075/3

# 1.    INTRODUCTION

## 1.1    Motivation and Objective

The Variable Thrust Engine (VTE), developed by TRW, for the Orbit Maneuvering Vehicle (OMV) uses a hypergolic propellant combination of Monomethyl Hydrazine (MMH) and Nitrogen Tetroxide (NTO) as fuel and oxidizer, respectively. The propellants are pressure fed into the combustion chamber through a single pintle injection element. The performance of this engine is dependent on the pintle geometry and a number of complex physical phenomena and their mutual interactions. The most important among these are:

1.  Atomization of the liquid jets into fine droplets;
2.  The motion of these droplets in the gas field;
3.  Vaporization of the droplets;
4.  Turbulent mixing of the fuel and oxidizer; and
5.  Hypergolic reaction between MMH and NTO.

Each of the above phenomena by itself poses a considerable challenge to the technical community. In a reactive flow field of the kind occurring inside the VTE, the mutual interactions between these physical processes tend to further complicate the analysis.

The reliable and optimum design of these engines requires a good understanding of the internal reactive flow field. Presently, the development of such engines is based on overall operation and performance characteristics. Some measurements are available for quantities, such as temperature and pressure at a few accessible locations.

The objective of this project is to develop a comprehensive mathematical modeling methodology to analyze the flow field within the VTE. This model can be used to obtain detailed information on the internal distributions of temperature, pressure, flow direction, and state/chemical composition. This information can then be used to optimize design parameters and thus improve the performance of the engine.

1

## 1.2    Project Tasks

This project is a three-year, three-phase effort to develop the analytical tool. Each phase is approximately of one year duration. The major tasks achieved during this study are:

### Phase I

1. Study of OMV/VTE Design and Physical Processes;
2. Code Adaptation;
3. Preliminary Computational Analysis; and
4. Formulation of the Impinging Injector Model.

A Phase I Interim Report[1] was prepared to document the results of the above mentioned activity.

### Phase II

1. Development of a Spray Model with Two-Liquid, Two Phase capability;
2. Implementation of Models for Finite Rate Evaporation and Heat Transfer;
3. Development of a Chemical Equilibrium Model to Simulate the Hypergolic Reaction between MMH and NTO;
4. Analysis of the Flow Field within the Heat Shield Area;
5. Stability analysis to estimate drop sizes; and
6. Analysis for Different Power Levels.

The details of the above mentioned tasks were documented in a Phase II Interim Report[2]. The results obtained during these two phases have been presented in a JANNAF Combustion Meeting[3] and in an AIAA meeting.[4]

### Phase III

1. Review of existing radiation heat transfer models and selection of a model for incorporation into the code;
2. Development of a turbulent dispersion model for the droplets;
3. Performing the OMV/VTE thrust chamber calculations using the new capabilities for different power levels (100%, 50%, and 10%);
4. Investigation of the effect of radiation on the flow field; and

2

5.    Assessment of current capabilities, identification of limitations, and recommendations for future work.

The details of the above mentioned tasks are described in this report. Section 2 describes the numerical approach and computational grid generation. The physical models are presented in Section 3. The validation of radiation and chemical equilibrium models is present in Section 4. The results of the simulations are discussed in Section 5. The conclusions from this study are presented in Section 6. Section 6 contains an assessment of current capabilities and recommendations for future work.

## 1.3    Accomplishments of the Project

The CFD code, REFLEQS, used in the first two Phases of this study[1,2] was based on the staggered grid approach of the finite-volume method. This traditional staggered grid approach is a well known and well established methodology. However, recent advances[5] in the colocated grid approach makes it more attractive and more suitable for flows in complex geometries. The staggered grid approach involves two control volumes: one for the scalar variables and the other for velocities. All the scalar variables are stored at the cell center and the velocities are stored at cell faces. In the colocated grid approach, all the variables share the same control volume and all the variables are stored at cell center. The two approaches have comparable accuracy and convergence rates. The colocated grid approach, however, has several advantages:

a.    The convection contribution to the coefficients in the discretized equations is same for all the variables. This increases computational efficiency for higher order schemes and for 3-D geometries.

b.    For complex geometries, cartesian velocity components can be used in conjunction with non-orthogonal coordinates, yielding simpler equations than when grid-oriented velocity components are employed.

c.    The colocated approach can be extended to multigrid approach. Recirculating flows often require very fine grids to achieve accurate solutions. The multigrid approach is a way to accomplish this at a

4075/3

reasonable computing cost. Thus, the colocated approach has advantages when these techniques are used.

d. The treatment of boundary conditions are relatively simple for colocated approach because of two reasons: no half cells are needed and the control volume faces coincide with boundaries.

The colocated grid approach has been implemented in the REFLEQS code during the third Phase of this study. This represents a major enhancement of the code capabilities.

The second major accomplishment is the development of a radiation model for BFC geometries. A literature survey was performed to select a suitable model for predicting radiative heat transfer in rocket engines. Most of the work reported in the literature on radiative heat transfer deal with orthogonal geometries and some of the methods reported cannot be extended to complex geometries. The discrete-ordinate radiation model, however, was found to be very suitable for extension to complex geometries. Also, the discrete-ordinate method can be used for strongly participating media such as the combustion gases in the VTE engine. The methodology for extending this method to BFC geometries is original and will be published in the literature in the near future. With the implementation of BFC radiation model in the code, the radiative heat transfer in rocket nozzles can be predicted more accurately. In addition to the spray model development, the equilibrium chemistry model developed during the second phase of the project has been validated with ODE and TDE predictions.

Finally, several enhancements were made in the spray model. The evaporation rates are predicted more accurately by including the effect of liquid saturation pressure variation with temperature. The droplet trajectory calculation for BFC geometries are made accurate by tracking the droplets in the physical plane. A droplet turbulent dispersion model has been included in the spray model. Various drop size distribution functions can be used in specifying the droplet initial conditions.

The design and development of VTE engine was mostly based on overall operation and performance characteristics. This study has provided a detailed knowledge of

4

what exactly happens in the combustion chamber and nozzle of VTE. This information can be used to optimize design parameters and thus improve the performance of engine.

## 2. COMPUTATIONAL APPROACH

This section describes the numerical approach, the geometry and flow conditions used in the calculations, and the code adaptation that was done for this study.

### 2.1    Numerical Approach

An advanced Computational Fluid Dynamics (CFD) code, REFLEQS[6], was used for the numerical simulation. The salient features of REFLEQS are given below.

1.  Finite-volume approach of solving Favre-averaged Navier-Stokes equations.
2.  Cartesian, polar, and non-orthogonal Body-Fitted Coordinates (BFC).
3.  Colocated (non-staggered) grid.
4.  Strong conservative form of momentum equations with Cartesian components as dependent variables.
5.  Pressure-based methodology for incompressible and compressible flows.
6.  Fully implicit and conservative formulation.
7.  Pressure-based solution algorithms, including SIMPLE, a variant of SIMPLEC, and non-iterative PISO algorithm for all flow speeds.
8.  Four differencing schemes: upwind, central (with damping terms), MUSCL, and third-order Osher-Chakravarthy.
9.  Steady-state and transient (second-order time-accurate) analysis capability.
10. Symmetric Whole-Field linear equation solver and Conjugate Gradient Squared solver.
11. Stationary and rotating grid systems.
12. Multi-component flows with heat and mass transfer, and chemical reactions.
13. Eulerian-Lagrangian approach for two-phase flows.
14. Range of turbulence models including k-ε model, Baldwin-Lomax model and the Low-Re model.
15. Discrete ordinate thermal radiation model.

Table 2-1 provides an updated list of features and capabilities of the REFLEQS code.

## 2.2 Geometry and Computational Grid

Figure 2-1a presents the overall configuration of a (VTE) in which the main combustor and nozzle are shielded by a conical heat shield. The internal surface of the heat shield is covered with a reflective insulation blanket for the main chamber and nozzle. During the engine operation in vacuum environment, the volume between the nozzle wall and the shield surface may be filled with recirculatory hot combustion products.

The VTE thrust chamber, shown schematically in Figure 2-1b consists of a cylindrical nozzle and an injector head. A single impinging injector is mounted axially at the center of the injector head. The engine is supplied with hypergolic propellants MMH (monomethyl-hydrazine $CH_3NHNH_2$) as fuel and NTO (Nitrogen Tetroxide ($N_2O_4$)) as oxidizer. The chamber external wall is cooled by radiation while the propellant spray flow produces a fuel rich environment adjacent to the inside wall and enhances its cooling.

The configuration of the OMV/VTE thrust chamber was obtained from detailed design drawings. The data from the drawings were used to generate a Body Fitted Coordinate (BFC) computational grid shown in Figure 2-2a. Figure 2-2b shows the magnified view of the combustor section. Figure 2-2c shows the magnified view of the pintle geometry. The computational grid in Figure 2-2a has 100 x 30 cells in the longitudinal and radial directions, respectively. Figure 2-3 shows the grid for the nozzle with the heat shield. The computational domain has been extended downstream of the nozzle exit to resolve the plume.

# Table 2-1. Capabilities and Features in the REFLEQS Code

| | | | CFDRC | | |
|---|---|---|---|---|---|
| ORGANIZATION | | | CFDRC | | |
| RESPONS. PERSON | | | S. Habchi/A. Przekwas | | |
| CODE NAME | | | REFLEQS | | |
| DIMENSIONS | | | 2D,3D | | |
| COORDINATES | CART/CYL/SPH/BODY FIT | | Bdy Fit(all) | | |
| TIME PROBLEM | STEADY/UNSTEADY | | Stdy, Unstdy | | |
| TYPE OF FLOW | INVISCID/VISCID | Inviscid, Viscid: Laminar/Turbulent | Invu. Vis(-/T) | | |
| | INCOMP/COMPRESSIBLE | Incomp, Comp: Sub/Tran/Super/Hyper | Incmp, Cmx(Sb/Tr/Sp) | | |
| EQUATIONS | CONSERV/NONCONSERV | | Consv | | |
| | MOMENTUM | N-S(Incomp/Comp),PNS,Euler,etc. | N-S | | |
| | ENERGY | | Yes | | |
| | SPECIES | Max. No. of species handled | Yes(4 step reaction) | | |
| | MULTI PHASES TRACKING | Eul-Eul,Eul-Lag, Statistic | E-L | 2 liq. | |
| | EQUATION OF STATE | Ideal,Real Gas | R.G.(7) | | |
| | TRANSPORT PROPERTIES | Viscosity,Conductivity-Table,Equation | Tabl.Eqn | | |
| PHYSICAL PROCESS | TURBULENCE MODELING | Zero/Mixing Length/Baldwin-Lomax),1-EQ, | B-L(TBD) | | |
| | | 2-EQ(X-L,KEHigh, KELow, etc.),LES,PDF, | KeH,KeL | | |
| | | Algebraic Stress/Reynolds Stress M | | | |
| | ATOMIZATION MODEL | Drop Size(Assumed/Calculated), Others | Assmd. Calcu | | |
| | VAPORIZATION MODEL | Droplet(Singl/Multi),Critical Region(Sub/Sup) | Droplet(S/M) | | |
| | CHEMISTRY MODEL | None,Equilibrium,Finite Rate,etc. | EQ,FR | | |
| | RADIATION MODEL | Stsm Source: Flame, Wall, etc. | Yes(6 flux eqn) | disc. ord. | |
| ROCKET PROPELLANT | TYPE | O2, H2,Hydrocarbon, Hypergolic, etc. | HC/Air,Hypergolic | | |
| | PHASES(FUEL/OX) | Single, Two(Gas,Liquid, Solid) | Sgl,T(G/G,G/L,L/L) | | |
| DISCRETIZATION | FDM/FVM/FEM/SPECTRAL/ETC. | | FVM | | |
| NUMERICAL SCHEME | VARIABLES BASED | Pressure Based, Density Based, Others | P, V | | |
| | DIFF. ACCURACY:TIME/SPATIAL | Time(1st,2nd)/Spatial(1st,2nd,Higher) | T(1st)/S(1st, 2nd) | T (1st, 2nd) | |
| | MULTI STEP/FACTORIZATION | MS(Yes,No)/FACT(Yes,No) | | | |
| | EXPLICIT | Leap/DuF-Frank,Lax-Wend,MacCormack,etc. | | | |
| | IMPLICIT | MacCormack,Beam-Warming,Briley-McDonald | Fully Implicit | | |
| | OTHERS: SPECIFY | Crank-Nicolson,ADI,TVD,ALE/ICE-ALE | TVD | | |
| | | Flux Correct Transport,Taylor-Galerkin,etc. | | | |
| | | SIMPLE&,PISO&,SOLA-VOF,etc. | SIMPLEC | SIMPLEC/PISO | |
| | MULTIGRID CAPABILITY | Yes/No | No | | |
| MATRIX SOLVER | DIRECT METHOD | TDMA,Block TDMA,Error Vector Prop.,etc. | Mod. Stone's solver | M. Stone, CGS | |
| | ITERATIVE METHOD | Line Iter.,Gauss-Seidel,SOR,etc. | | | |
| | | Conjugate Gradient/Residue Method | | | |
| GRID | SEPARATE (NAME) | EAGLE,Grid Generation Package,etc. | EAGLE,GGP(out) | | |
| | INTERNAL | Stagg./Non-Staggered,Orthog/Non-Orthog, | Ortho/Northo | NS Ort/Nonort | |
| | | Struct/Unstructured,Adaptive Grid,Multi zone | Strct | | |
| | TECHNIC USED | FEM,Algebraic,Differential Eq'n | Algbr | | |
| INLET/WALL | INLET CONDITIONS | Constant,Time Varying,Characteristic | Const, TimeVar | | |
| BOUNDARY COND. | WALL BOUNDARY | No slip/Slip,Stationary/Moving | User Select | | |
| | | Adiabatic,Isotherm,Constant Flux,etc. | | User Select | |
| | | Smooth/Rough Surface | Handl Interior B.C. | | |
| | | Droplet wall interaction(Adhere/Bounce) | Adh,Bounce | | |
| PROGRAM CAPABILITY | INCOMPRESSIBLE FLOWS | Reynolds No. Ranges | Swirl, Rotation flow | | |
| (Experienced) | COMPRESSIBLE FLOWS | Mach No. Ranges | 0 - 65 | | |
| | INTERNAL FLOW | Separating,Recirculating,Cavity Flows,etc. | Separ,Recirc,Cavity | | |
| | | Combustion Chamber,Nozzle | Combustor,Nozz | | |
| | INJECTION | Element: Coaxial,Impinging | Yes(7) | | |
| | | Process: Atomization,Mixing,Vaporization | Atomz, Vapor,Mix | | |
| | PERFORMANCE PREDICTION | Thrust Chamber: Isp,Therm Props,Dynamics | Thrust,Isp,Dyn prop | | |
| | MISC. | Other than Thrust Chamber | Duct | | |
| CODE VALIDATION | UNIQUE CASES | No. Solved(Include benchmark cases) | 40 | 70 | |
| | CASES PUBLISHED | Number | 30 | 50 | |
| | THRUST CHMBR RELATED | Number | 4 | 7 | |
| PRE/POST PROCESSOR | DEVELOPED | In-house, By Others | Inhouse | | |
| | OPERATION | Batch,Interactive | Batch,Interact | | |
| | GRAPHICS | Display,Plot3D,Self,etc. | Plot3D,XYPLOT | ACE PLOT, CFD-VIEW | |
| PROGRAM | DOCUMENTATION | Manual-Engineering Program,User | Eng,Prog,User | | |
| | AVAILABILITY | Proprietary,Sale Protect(SBIR),Pub. domain | Prot | | |
| COMPUTER SYSTEM | MAIN FRAME | Cray, IBM,Cyber,etc. | Cray, IBM | | |
| | MINI COMPUTER | Convex,Alliant,Vax,etc. | Alliant,Ardent,Vax | | |
| | WORKSTATION | Sun,Apollo,Tek,SiliconG,etc. | Sun | | |
| MISCELLANEOUS | CODE EXPERIENCE | No. of years Used | 4 Yrs | 6 | |
| | CODE ORIGIN | In-house/Acquired: Original code name | Inhouse | | |
| | VECTORIZATION | Programed (or vectorization(Yes/No) | Yes | | |

Survey Date : October, 1990 (Except **)          Note:

8
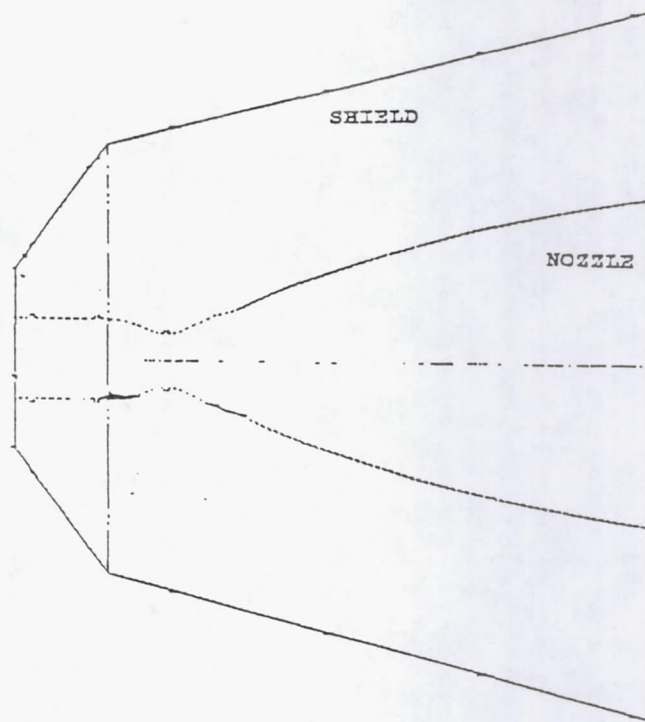
Figure 2-1(a). Schematic of VTE Combustion Chamber and Nozzle
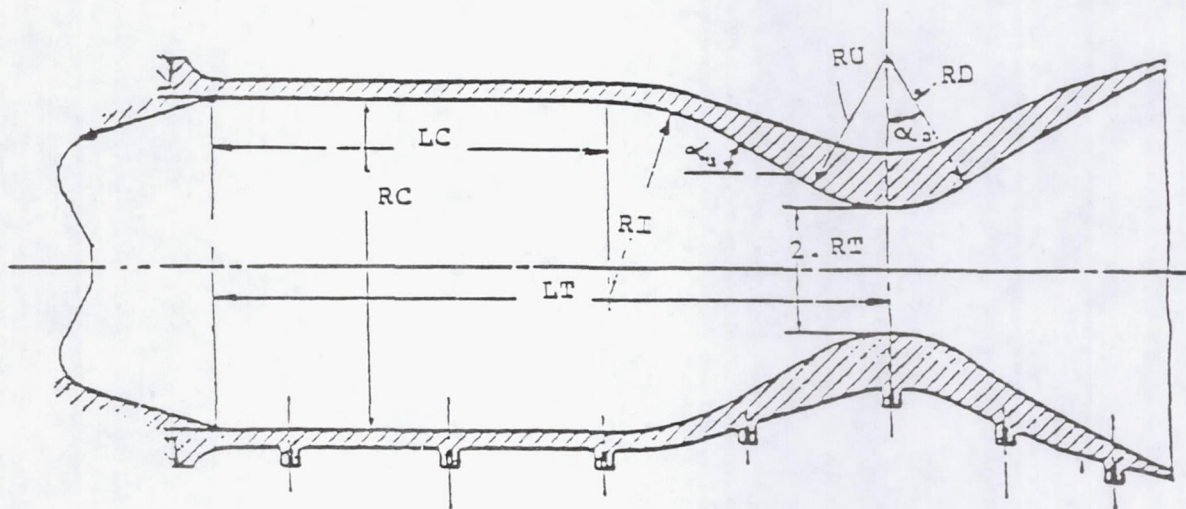


Figure 2-1(b). Schematic of VTE Thrust Chamber

9
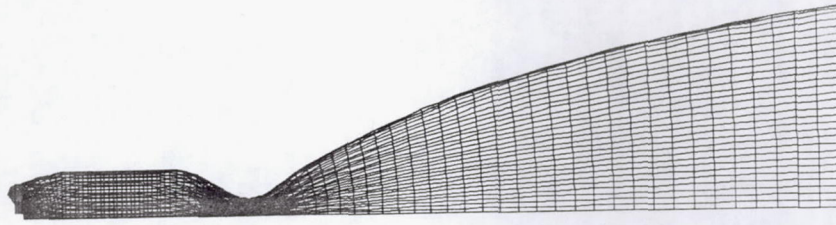
(a)  Computational Grid for the OMV/VTE Combustor and Nozzle
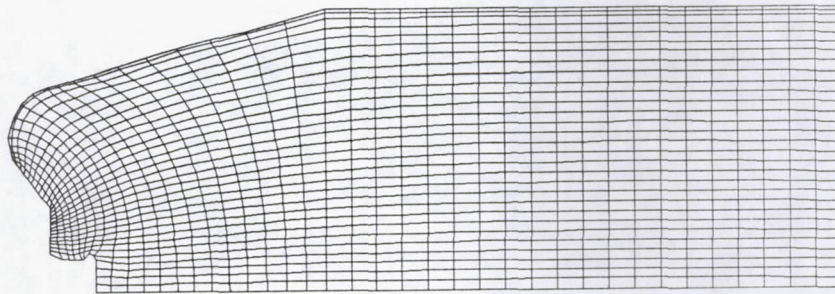


(b)  Magnified View of the Combustor Grid
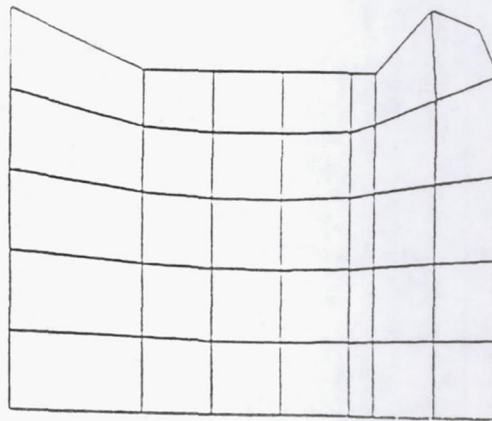


(c)  Magnified View of the Pintle Grid

Figure 2-2.  Computational Grid for the OMV/VTE Engine

10
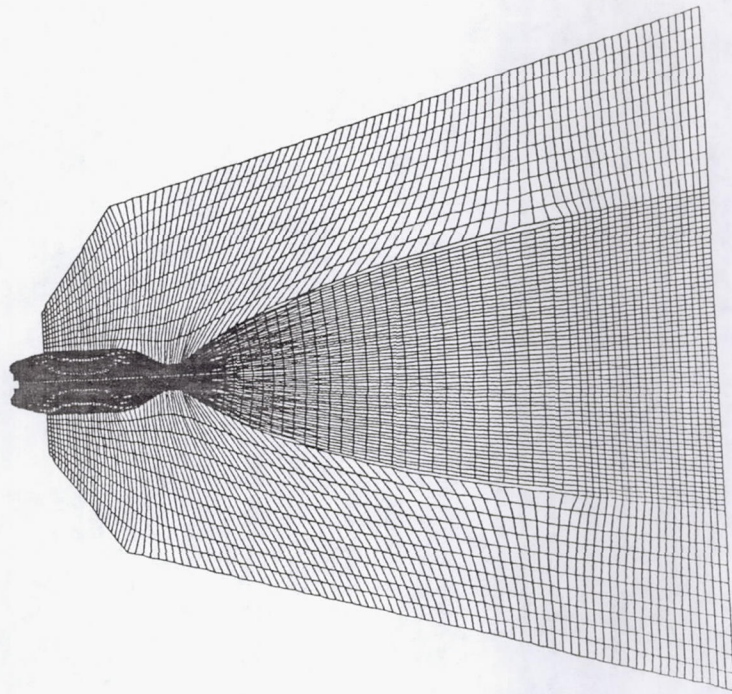
Figure 2-3. Computational Grid for the OMV/VTE Engine with Heat Shield

## 2.3    Boundary and Flow Conditions

A constant mass flow rate is prescribed at the oxidizer and fuel inlets of the VTE combustor/nozzle. The density of the incoming propellants is calculated using the reference chamber pressure an inlet temperature of 300°K. For liquid injection, the drop sizes are prescribed according to a presumed distribution function. The droplets are initially located approximately around the point of impact of the two liquid jets. The droplets are injected at a temperature of 300°K. Since the flow at the exit is supersonic, the pressure at the exit plane is extrapolated from the cell center pressure. The walls of the VTE combustor/nozzle are treated as adiabatic. A standard k-ε model is used to model the turbulent flow field. A chemical equilibrium model with thirteen species is used to simulate the hypergolic reaction between MMH and NTO.

Physical properties for the propellants (MMH and NTO) are obtained from data provided by TRW. Some of the properties of these propellants are listed in Table 2-2. The mass flow rates of the propellants and the injection areas are obtained for operation at the 100% power level. For reference, the conditions used in the

11

computations are summarized below in Table 2-3. The mass flow rates and chamber pressure are proportionately reduced for the lower power levels.

Table 2-2. Physical Properties of MMH and NTO

| Property | MMH | NTO |
|---|---|---|
| Density, $kg/m^3$ | 870.0 | 1433.0 |
| Boiling Point, °K | 360 | 300 |
| Saturation Pressure, $N/m^2$ | $6.6 \times 10^3$ | $1.2 \times 10^5$ |
| Heat of Vaporization,KJ/kg | 875.0 | 414.0 |
| Heat Capacity,J/kg°K | 3000.0 | 1580.0 |
| Surface Tension, N/m | $33.9 \times 10^{-3}$ | $25.1 \times 10^{-3}$ |

4075/3 12-1

Table 2-3. Flow and Reaction Parameters

| No. | Power Level | Flow Rate (kg/s) MMH | NTO | Pressure (psia) |
|---|---|---|---|---|
| 1 | 100% | .089 | .146 | 100 |
| 2 | 50% | .0445 | .073 | 50 |
| 3 | 10% | .0089 | .0146 | 10 |

4075/3 12-2

## 2.4    Code Modification and Adaptation

The code was modified during this study to include the following models:

a.    a 2-liquid, two-phase Eulerian-Lagrangian spray model;

b.    a droplet turbulent dispersion model;

c.    a chemical equilibrium model to simulate the hypergolic reaction between MMH and NTO;

d.    a thermal radiation heat transfer model; and

e.    a linear stability analysis model to predict drop sizes.

The details of each of these models are discussed in the following sections.

12

## 3. PHYSICAL MODELS

This section presents detailed technical descriptions of the physical models developed/adopted during this study.

### 3.1 Chemical Equilibrium Model

In the previous phases of this project, the hypergolic reaction between MMH and NTO was modeled using single global step instantaneous and finite-rate chemistry models. It was shown that these models overpredict the flame temperature. The reason for this is that the actual reaction between MMH and NTO involves about 200 species and several reaction steps. Detailed modeling of all the species and reaction steps would be computationally very expensive. It was felt that a chemical equilibrium model would be more appropriate in terms of providing reasonable accuracy as well as computationally efficient. After reviewing the literature, the equilibrium model based on the element potential method was incorporated into the REFLEQS code. This model is very general and thus can be applied to any propellant combinations provided that important species in the reactions are included. This model is very similar to the equilibrium model in the ODE code.

The chemical equilibrium model proposed by Morgan and Meintjes[5] is described below. This method is based on calculating the element potentials or the element activities and is an indirect approach of minimizing the Gibbs function of the system.

The chemical potential of any species "$j$" can be written as:

$$\mu_j = \mu_j^o + RT ln\left(\frac{p_j}{p_o}\right)$$

(3.1)

where $\mu_j$ = chemical potential, $\mu_j^o$ = standard state Gibbs function, $p_o$ = atmospheric pressure and $p_j$ = partial pressure of species '$j$'.

$$p_j = \frac{n_j}{n}p$$

(3.2)

13

where $n_j/n$ is the mole fraction of species '$j$', $p$ is the total pressure of the mixture and $p_o$ is the atmospheric pressure.

The chemical potential "$\mu_j$" can be written as:

$$\mu_j = \sum_{i=1}^{I} a_{ij}\,\mu_i \tag{3.3}$$

where $\mu_i$ is the chemical potential of atomic element $i$ and $a_{ij}$ is the number of atoms of '$i$' in species '$j$'. Substituting into Equation (3.1),

$$\frac{1}{RT} \sum_{ni=1}^{I} a_{ij}\,\mu_i = \frac{\mu_j^o}{RT} + \ln\left(\frac{n_j}{n}\,\frac{p}{p_o}\right) \tag{3.4}$$

From the equation of state,

$$\frac{p}{n} = \frac{RT}{V} \tag{3.5}$$

Therefore,

$$\frac{1}{RT} \sum_{i=1}^{I} a_{ij}\,\mu_i = \ln\left(\frac{RT}{p_o}\right) + \ln\left(\frac{n_j}{V}\right) + \frac{\mu_j^o}{RT} \tag{3.6}$$

where $n_j/V$ = molar concentration = $c_j$.

Rewriting Equation (3.6),

$$\ln c_j = -\frac{\mu_j^o}{RT} - \ln\left(\frac{RT}{p_o}\right) + \sum_{i=1}^{I} a_{ij}\,\lambda_i \tag{3.7}$$

14

where $c_j = n_j/v$ and $\lambda_i = \mu_i/RT$.

Equation (3.7) can be written as:

$$ln\ c_j = ln\ R_j + \sum_{i=1} a_{ij}\ ln\ Z_i \tag{3.8}$$

where

$$R_j = \frac{P_o}{RT}\ exp\left(-\frac{\mu_j^o}{RT}\right) \tag{3.9}$$

and

$$Z_i = e^{\lambda_i}\ \text{(an element variable)}$$

Equation (3.8) is simplified as:

$$c_j = R_j \prod_{i=1}^{I} \left(Z_i\right)^{a_{ij}} j = 1,...J \tag{3.10}$$

Since atoms of each element are conserved, we can write:

$$\sum_{j=1}^{I} a_{ij}\,c_j = b_i\,,\,i = 1,...\,I \tag{3.11}$$

where $b_i$ is the total number of atoms of element "$i$" in all species.

Equations (3.55) and (3.56) form the basis of this formulation. Substituting Equation (3.55) into (3.56) we get

$$\sum_{j=1}^{J} \left\{ a_{ij}\,R_j \prod_{m=1}^{I} \left(Z_m\right)^{a_{mj}} \right\} - b_i = 0\,,\,i = 1,...I \tag{3.12}$$

15

Thus we have '$I$' non-linear algebraic equations for the '$I$' unknown values of $Z_i$. The values of $c_j$ are calculated from the solved values of $Z_i$ (using Equation 3.10). The temperature is calculated from $c_j$ and then the new values of $R_j$ are calculated. The system is solved again for new values of $Z_i$ and so on until convergence is achieved.

## 3.2    Radiation Model

A number of numerical techniques[8,9] are available for solving the equation governing the transfer of thermal radiation.  The most widely used among them are listed below.

a.    Hottel's Zone method[10]
b.    Flux method[11]
c.    P-N approximation method[12]
d.    Monte-Carlo method[13]
e.    Discrete-transfer method[14]
f.    Discrete-ordinate method[15-17]

Hottel's zone method was the first general numerical procedure developed to handle the radiative transfer equation.  It has been widely used to estimate the radiation transfer in the absence of detailed knowledge of the flow and reaction. This method involves the use of exchange factors, which needs to be worked out in advance for complex geometries.  The disadvantage of this method is that it is very uneconomical and not suited for complex configurations with strongly participating media.  The flux methods involve a differential approximation to the radiative transfer equation.  This method is computationally efficient and has, therefore, been widely used in general combustion problems.  However, this method suffers from inadequate accuracy and the difficulty to extend to complex geometries.  Compared to this method, the P-N approximation method is more accurate.

Among all the existing numerical treatments for radiative heat transfer, the Monte-Carlo method is the most accurate method. In this method, the randomly chosen energy releases are tracked through the combustion chamber for their lifetimes. Unfortunately, this method is computationally expensive.  The discrete-transfer

method, on the other hand, is economical and can be applied in a straightforward manner to complex geometries. This method, however, cannot treat the scattering by the medium, containing droplets and soot particles, and hence is not suitable for combustor applications.

After comprehensive review of all the methods, it has been found that the discrete-ordinate model is well suited for radiation prediction in rocket combustion chambers. There are several advantages of this method. Firstly, the discrete-ordinate method can be easily extended to polar and complex geometries. Secondly, the evaluation of the in-scattering term is relatively simple. Also, the boundary conditions can be imposed more accurately at inlets and exits. Finally, this method is accurate and can be easily coupled with CFD codes, based on the finite volume approach. The governing equations and the solution procedure for this method are described below.

### 3.2.1 Governing Equations

The integro-differential radiative heat transfer equation for an emitting-absorbing and scattering gray medium can be written as[13]

$$(\Omega \cdot \nabla) I(r, \Omega) = -(k + \sigma) I(r, \Omega) + k I_b(r) + \frac{\sigma}{4\Pi} \int_{\Omega'=4\Pi} I(r, \Omega') \phi(\Omega' \to \Omega) d\Omega' \tag{3.13}$$

where $\Omega$ is the direction of propagation of the radiation beam, $I$ is the radiation intensity, which is a function of both position $(r)$ and direction $(\Omega)$, $k$ and $\sigma$ are the absorption and scattering coefficients respectively. $I_b$ is the intensity of black body radiation at the temperature of the medium, $\phi$ is the phase function of the energy transfer from the incoming $\Omega'$ direction to the outgoing direction $\Omega$. The term on the left hand side represents the gradient of the intensity in the specified direction $\Omega$. The three terms on the right hand side represent the changes in intensity due to absorption and out-scattering, emission and in-scattering respectively.

The boundary condition for solving the above equation may be written as

$$I(r, \Omega) = \varepsilon I_b(r) + \frac{\rho}{\pi} \int_{n \cdot \Omega' < 0} |n \cdot \Omega'| I(r, \Omega) d\Omega' \tag{3.14}$$

17

where $I$ is the intensity of radiant energy, leaving a surface at a boundary location, $\varepsilon$ is the surface emissivity, $\rho$ is the surface reflectivity, and $n$ is the unit normal vector at the boundary location.

In the discrete-ordinate method, Equations (3.13) and (3.14) are replaced by a discrete set of equations for a finite number of ordinate directions. The integral terms on the right hand side of the above equations are approximated by summation over each ordinate. The discrete-ordinate equations may then be written as,

$$\mu_m \frac{\partial I_m}{\partial x} + \xi_m \frac{\partial I_m}{\partial y} = -(k + \sigma) I_m + k I_b + \frac{\sigma}{4\Pi} \sum_{m'} w_{m'} \phi_{m'm} I_{m'} \; ; m = 1, ...M \tag{3.15}$$

For cylindrical polar geometries, the discrete-ordinate equation may be written as,

$$\frac{\xi_m}{r} \frac{\partial (r I_m)}{\partial r} - \frac{1}{r} \frac{\partial (\eta_m I_m)}{\partial \phi} + \mu_m \frac{\partial I_m}{\partial z} = -(k + \sigma) I_m + k I_b + \frac{\sigma}{4\Pi} \sum_{m'} w_{m'} \phi_{m'm} I_{m'} \; ; m = 1, ...M \tag{3.16}$$

where the second term on the left hand side represents the angular intensity redistribution. It accounts for the change in the direction cosines as a beam travels in a straight line.

The different boundary conditions, required to solve this equation, are given as:

Wall Boundary

$$I_m = \varepsilon I_b + \frac{\rho}{\pi} \sum_{\mu'_m < 0} w'_m |\mu'_m| I'_m \; ; for\ west\ boundaries$$

$$I_m = \varepsilon I_b + \frac{\rho}{\pi} \sum_{\mu'_m > 0} w'_m \mu'_m I'_m \; ; for\ east\ boundaries$$

$$I_m = \varepsilon I_b + \frac{\rho}{\pi} \sum_{\xi'_m < 0} w'_m \left| \xi'_m \right| I'_m \; ; \textit{for south boundaries}$$

$$I_m = \varepsilon I_b + \frac{\rho}{\pi} \sum_{\xi'_m > 0} w'_m \, \xi'_m I'_m \; ; \textit{for north boundaries}$$

(3.17)

Symmetry Boundary

$$I_m = I_{m'} \; ; \mu_{m'} = -\mu_m \; \textit{for east and west boundaries;}$$

$$I_m = I_{m'} \; ; \xi_{m'} = -\xi_m \; \textit{for south and north boundaries}$$

(3.18)

Inlet and Exit Boundary

$$I_m = 0$$

(3.19)

In the above equations, $m$ and $m'$ denote the outgoing and incoming directions, respectively. For a particular direction, denoted by $m$, the values $\mu$ and $\xi$ are the direction cosines along the x and y directions. These equations represent $m$ coupled partial differential equations for the $m$ intensities, $I_m$. In the present code, only the $S_4$ approximation, *i.e.* 12 ordinate directions, is considered. Table 3-1 lists the values of the direction cosines and the associated weights.

Equation (3.15) can be cast in a fully conservative form for a general BFC coordinate system as

$$\frac{\partial}{\partial x'} \left[ \mu_m I_m J F_{1x} + \xi_m I_m J F_{1y} \right] + \frac{\partial}{\partial y'} \left[ \mu_m I_m J F_{2x} + \xi_m I_m J F_{2y} \right]$$

$$= J \left[ -(k + \sigma) I_m + k I_b + \frac{\sigma}{4\Pi} \sum w_{m'} \phi_{m'm} I_{m'} \right]$$

(3.20)

where $x'$ and $y'$ are the local grid coordinate directions, $J$ is the Jacobian of the coordinate transformation and

19

$$F_{1x} = \frac{\partial x'}{\partial x}$$

$$F_{1y} = \frac{\partial x'}{\partial y}$$

$$F_{2x} = \frac{\partial y'}{\partial x}$$

$$F_{2y} = \frac{\partial y'}{\partial y}$$

(3.21)

Table 3-1. Direction Cosines and the Associated Weights for the $S_4$ Approximation

| Direction Number | Direction Cosines | | | Weight $w_m$ |
|---|---|---|---|---|
| | $\mu_m$ | $\xi_m$ | $\eta_m$ | |
| 1 | -0.908248 | -0.295876 | .295876 | $\pi/3$ |
| 2 | -0.908248 | 0.295876 | .295876 | $\pi/3$ |
| | | | | |
| 3 | -0.295876 | -0.908248 | .295876 | $\pi/3$ |
| 4 | -0.295876 | -0.295876 | .908248 | $\pi/3$ |
| 5 | -0.295876 | 0.295876 | .908248 | $\pi/3$ |
| 6 | -0.295876 | 0.908248 | .295876 | $\pi/3$ |
| | | | | |
| 7 | 0.295876 | -0.908248 | .908248 | $\pi/3$ |
| 8 | 0.295876 | -0.295876 | .908248 | $\pi/3$ |
| 9 | 0.295876 | 0.295876 | .908248 | $\pi/3$ |
| 10 | 0.295876 | 0.908248 | .295876 | $\pi/3$ |
| | | | | |
| 11 | 0.908248 | -0.295876 | .295876 | $\pi/3$ |
| 12 | 0.908248 | 0.295876 | .295876 | $\pi/3$ |

4075/3 t3-1

Equation (3.16) can be integrated over the control volume, shown in Figure 3-1, to obtain

$$\mu_m \left( A_e I_{m_e} - A_w I_{m_w} \right) + \xi_m \left( A_n I_{m_n} - A_s I_{m_s} \right) + \left( A_n - A_s \right) \frac{\left[ \gamma_{m+1/2} I_{P,\, m+1/2} - \gamma_{m-1/2} I_{P,m-1/2} \right]}{w_m}$$

$$= -(k + \sigma) \forall I_{mP} + k \forall I_{bp} + \forall \frac{\sigma}{4\Pi} \sum_{m'} w_{m'} \phi_{m'm} I_{m'p}$$

(3.22)

where the coefficients $\gamma$ are evaluated from the recurrence relation

$$\gamma_{m+1/2} = \gamma_{m-1/2} - \xi_m w_m \tag{3.23}$$

In the above equation $A$ denotes the cell face area and $\forall$ denotes the cell volume and subscripts $w$, $e$, $s$, $n$, $P$ denote the west, east, south, north, and cell center, respectively. Figure 3-1 shows a sketch of the control volume.



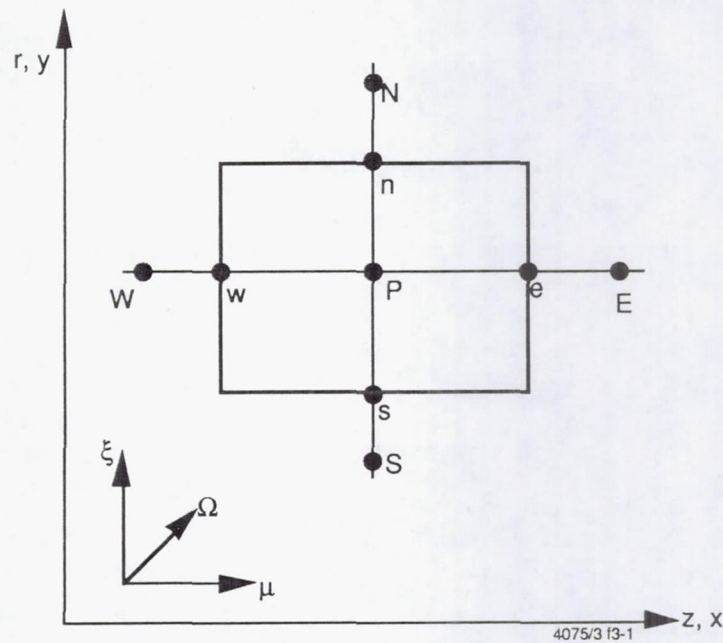Figure 3-1. Sketch of the Control Volume

The in-scattering term on the right hand side of this equation contains the phase function $\phi$, which can be prescribed for both isotropic and anisotropic scattering by the medium. For a linear anisotropic scattering, the phase function may be written as,

$$\phi_{m'm} = 1 \cdot 0 + a_o \left[ \mu_m \mu_{m'} + \xi_m \xi_{m'} + \eta_m \eta_{m'} \right] \tag{3.24}$$

21

where $a_0$ is the asymmetry factor that lies between -1 and 1. The values -1,0,1 denote backward, isotropic and forward scattering, respectively.

### 3.2.2 Solution Procedure

Equations (3.22) involves 5 intensities, out of which 2 intensities are known from the boundary conditions. The other cell face intensities can be eliminated in terms of the cell center intensity by a spatially weighted approximation. For example, if the east and north cell face intensities are unknown, they can be eliminated in terms of the cell center intensity by using

$$I_{m_n} = \frac{I_{m_p} - (1 - \alpha)\, I_{m_s}}{\alpha} \tag{3.25a}$$

$$I_{m_e} = \frac{I_{m_p} - (1 - \alpha)\, I_{m_w}}{\alpha} \tag{3.25b}$$

where $\alpha$ is the weighting factor. $\alpha=1$ yields a upwind differencing scheme and $\alpha=1/2$ yields a central differencing or the "diamond differencing" scheme. Substituting Equation (3.25) into the integrated discrete-ordinate equation results in a algebraic equation for the cell center intensity,

$$I_{m_p} = \frac{\mu_m\, A\, I_{m_w} + \xi_m\, B\, I_{m_s} + S_1 - S_2}{\mu_m A_N + \xi_m A_S + \alpha\,(k + \sigma)\,\forall} \tag{3.26}$$

where

$$A = A_e(1 - \alpha) + A_w \alpha$$
$$B = A_n(1 - \alpha) + A_S \alpha$$
$$S_1 = \alpha \, k \, \forall \, I_{bp}$$
$$S_2 = \alpha \, \forall \, \frac{\sigma}{4\Pi} \, w_{m'} \, \phi_{m'm} \, I_{m'P}$$

Equation (3.26) is appropriate, when both the direction cosines are positive and the direction of integration proceeds in a direction of increasing x and y. For a negative direction cosine, the direction of integration is reversed, and the integration sweep is started from the appropriate corner of the domain. Thus, for each set of direction cosines, the intensities at all the cell centers are obtained by marching in the appropriate direction. This procedure is repeated for all the ordinate directions. The in-scattering term is evaluated explicitly by using the previous iteration values, thus decoupling the m ordinate equations.

Assuming local radiative equilibrium, the source term for each computational cell *i.e.* the net radiative heat flux, is given by,

$$S = \forall \, k \sum_m I_m \, w_m - \forall \, 4\Pi \, k \, I_b \tag{3.27}$$

This source term is added to the gas phase energy equation. The gas phase equations and the radiative transfer equations are solved in an iterative manner.

### 3.3    Spray Model

There are two approaches for modeling sprays: (a) Eulerian-Eulerian; and (b) Eulerian-Lagrangian. In the Eulerian-Eulerian approach, the droplet phase is treated as a continuum. Thus, the liquid phase equations are similar to the gas phase equations. These two sets of equations are solved in a strongly coupled manner. In the Eulerian-Lagrangian approach, individual drop parcels are tracked until their lifetime in a Lagrangian frame of reference. The gas phase equations are coupled with the liquid phase equations through droplet source/sink terms. The major

assumption used in this approach is that the volume occupied by the liquid phase is negligibly small when compared to the cell volume. This assumption does not hold in the dense spray region. Thus, the Eulerian-Eulerian approach is more accurate is in this respect. However, the Eulerian-Eulerian approach suffers from other difficulties such as boundary condition treatment, smearing of the liquid phase, effect of gas phase pressure gradient, *etc*. Moreover, in typical reacting flow problems, the spray region is small when compared to the flow domain. Hence, the Eulerian-Eulerian approach is computationally inefficient. Due to these reasons, the Eulerian-Lagrangian approach is widely used and it is implemented in the REFLEQS code.

The droplet equations of mass, momentum and energy are solved in a Lagrangian frame of reference moving with the droplets. These solutions are used to calculate the source/sink terms for the corresponding gas phase equations.

The equation of motion for the droplet is written as[19]:

$$m_d \frac{d\mathbf{v}}{dt} = C_D \rho (\mathbf{U} - \mathbf{v}) |\mathbf{U} - \mathbf{v}| \frac{A_d}{2} - \nabla p \cdot V_d + m_d \frac{v_\theta^2}{r} \mathbf{e}_r - m_d \frac{v_r v_\theta}{r} \mathbf{e}_\theta + m_d \mathbf{g} \qquad (3.28)$$

where $m_d$ is the mass of the droplet and $\mathbf{v} = v_x \mathbf{e}_x + v_r \mathbf{e}_r + v_\theta \mathbf{e}_\theta$ its velocity vector. $v_x$, $v_r$ and $v_\theta$ are the axial, radial and swirl components of the velocity. $C_D$ is the drag coefficient and $\rho$, $\mathbf{U}$, and $p$ are the density, velocity, and pressure of the gas, respectively. $A_d$ is the droplet surface area, and $V_d$ is the droplet volume. For a spherical droplet, $A_d = \pi d^2$ and $V_d = (\pi d^3/6)$, where d is the droplet diameter. $\mathbf{g}$ is the gravity vector, and $r$ is the radial position of the droplet. Equation (3.28) accounts for the acceleration/deceleration of the droplet, due to combined effects of drag with gas, local pressure gradients, centrifugal and Coriolis forces, and body forces, such as gravity. The centrifugal force term appears only in the radial velocity equation, and the coriolis force term appears only in the swirl velocity equation.

The drag coefficient, $C_D$, for the droplet is based on the local Reynolds number, evaluated as:

24

$$Re = \frac{\rho |U - v| d}{\mu} \tag{3.29}$$

where $\mu$ is the dynamic viscosity of the gas. The following correlations have been found to be valid for different ranges of Reynolds numbers:

$$C_D = \frac{24}{Re} \qquad \text{for Re} < 1$$

$$C_D = \frac{24}{Re} \left[1 + 0.15 Re^{0.687}\right] \quad \text{for } 1 < Re < 10^3$$

$$C_D = 0.44 \qquad \text{for Re} > 10^3$$

$$\tag{3.30}$$

Substituting for $C_D$ into Equation (3.28),

$$\frac{dv}{dt} = \frac{18\mu f}{\rho_d d^2}(U - v) - \frac{\nabla p}{\rho_d} + \frac{v_\theta^2}{r} e_r - \frac{v_r v_\theta}{r} e_\theta + g \tag{3.31}$$

where $\rho_d$ is the droplet liquid density and $f = C_D Re/24$. The droplet locations are determined from the velocities as:

$$\frac{dR}{dt} = v \tag{3.32}$$

where $R$ is the position vector of the droplet.

The mass conservation equation for the droplet is given by:

$$\frac{dm_d}{dt} = -\text{Sh}\,(\rho D)\,\pi d\,(x_v - x_\infty) \tag{3.33}$$

where Sh is the Sherwood number, and $D$ is the mass diffusion coefficient for the gas. $x_v$ and $x_\infty$ are the vapor mass fractions at the droplet surface and the free

stream, respectively. In this model, $x_v$ is calculated from expressions for the vapor pressure as a function of droplet temperature. The Sherwood number is obtained from the following expression:

$$Sh = 2 + 0.6Re^{0.5} S_c^{0.333} \qquad (3.34)$$

where $S_c$ is the Schmidt number. Since $m_d = \rho_d \pi d^3 / 6$, the mass equation for the droplet is rewritten in terms of its diameter:

$$\frac{d(d)}{dt} = -2Sh\left(\rho D\right)\frac{x_v - x_\infty}{\rho_d d}$$

$$\qquad (3.35)$$

The energy equation for the droplet is written as:

$$m_d C_d \frac{dT_d}{dt} = \dot{q} + L\left(\frac{dm_d}{dt}\right) \qquad (3.36)$$

where $\dot{q}$ is the sensible heat transferred to the droplet and $T_d$ is the droplet temperature. $L$ is the latent heat of vaporization for the droplet fluid and $C_d$ is the specific heat of the droplet. $\dot{q}$ is calculated as:

$$\dot{q} = Nu\,\pi kd\left(T_g - T_d\right) \qquad (3.37)$$

where $k$ and $T_g$ are the thermal conductivity and temperature of the gas, respectively. The Nusselt number, Nu, is obtained from the following correlation:

$$Nu = 2 + 0.6Re^{0.5} Pr^{0.333} \qquad (3.38)$$

where Pr is the Prandtl number. Substituting the above expressions into Equation (3.36), the energy equation is rewritten as:

$$\frac{dT_d}{dt} = \frac{T_g - T_d}{\theta} - \frac{Q_L}{\theta}$$

$$\qquad (3.39)$$

26

where

$$Q_L = \frac{L \, \mathrm{Sh} \, (\rho D) \left( x_v - x_\infty \right)}{\mathrm{Nu} k} \tag{3.40}$$

$$\theta = \frac{\rho_d d^2 C_d}{6 \mathrm{Nu} k} \tag{3.41}$$

If the droplet temperature is below its boiling point, Equation (3.35) is used as the mass conservation equation. Once the droplet attains its boiling point, the mass conservation equation is obtained by setting the left hand side of Equation (3.36) to zero, *i.e.*, the droplet temperature cannot exceed its boiling point. Therefore,

$$\frac{dm_d}{dt} = -\frac{\dot{q}}{L} \tag{3.42}$$

This equation implies that all the heat transferred from the gas is used to vaporize the droplet.

### 3.3.1 Calculation of Droplet Source/Sink Terms

The solutions to the droplet equations provide sources/sinks to the gas phase conservation equations. The sources/sinks are assigned to the particular cell (in the Eulerian gas phase) in which the droplet is located. The calculation of the source/sinks is as follows.

The mass of the droplet is continuously monitored along its trajectory. The source/sink term for a cell is given as:

$$\Delta \dot{m} = \rho_d \pi \dot{n} \sum_i \frac{\left( d_i^3 \right)_{\mathrm{in}} - \left( d_i^3 \right)_{\mathrm{out}}}{6} \tag{3.43}$$

27

the summation takes place over all the droplets located in the given cell. The subscripts "in" and "out" refer to cell inlet and outlet conditions, and $\dot{n}$ is the droplet number density. Similarly the momentum source/sink term is evaluated as:

$$\Delta\dot{\mathbf{M}} = \rho_d \pi \dot{n} \sum_i \frac{\left(\mathbf{v}_t d_i^3\right)_{\text{in}} - \left(\mathbf{v}_t d_i^3\right)_{\text{out}}}{6} \tag{3.44}$$

This includes the effects of frictional interactions with the gas. The momentum source term is a vector. The energy source/sink term is given as:

$$\Delta\dot{E} = \Delta\dot{m}h_v - \dot{n}\sum_i \dot{q}_i \tag{3.45}$$

where $h_v$ is the enthalpy of the vapor at the vaporization temperature and $\dot{q}_i$ is the heat transfer from the gas to the droplet (calculated according to Equation (3.37)).

### 3.3.2 Governing Equations for the Gas Field

The mass conservation for the flow can be represented by the continuity equation. This formulation accounts for a variable density flow field:

$$\nabla \cdot \rho\mathbf{u} = \dot{S}_\rho \tag{3.46}$$

where

$$\dot{S}_\rho = \frac{\Delta\dot{m}}{\forall} \tag{3.47}$$

$\Delta\dot{m}$ is obtained from Equation (3.43), and $\forall$ is the volume of the cell, in which the mass addition takes place. $\rho$ is the density of the fluid, and $\mathbf{u}$ is the velocity vector. The mass conservation for individual species may be written as:

28

$$\nabla \cdot \rho \mathbf{u} Y_k = \nabla \cdot (D_k \nabla Y_k) + W_k + \dot{S}_k \tag{3.48}$$

where $\dot{S}_k = \dfrac{\Delta \dot{m}_k}{\forall}$ and $Y_k$ is the mass fraction of specie, $k$, and $W_k$ is a source term, consisting of reaction rate expressions. $\Delta \dot{m}_k$ is the mass of species $k$ added, due to vaporization.

The momentum conservation equation for the flow is written as:

$$\nabla \cdot \rho \, \mathbf{u} \mathbf{u} = - \nabla p - \nabla \cdot \tau + \rho \mathbf{g} + \dot{\mathbf{S}}_m \tag{3.49}$$

where $\dot{\mathbf{S}}_m = \dfrac{\Delta \dot{\mathbf{M}}}{\forall}$ , and $\tau$ is the stress tensor equal to $-\mu(\nabla u + \nabla u^T)$. $\Delta \dot{\mathbf{M}}$ is obtained from Equation (3.44). It is assumed that the gas behaves as a Newtonian fluid. The energy conservation equation for the system is given by:

$$\nabla \cdot \rho \mathbf{u} \left( h + |\mathbf{u}|^2/2 \right) = \nabla \cdot \lambda \nabla T - \nabla \cdot (\mathbf{u} \cdot \tau) + \dot{S}_e \tag{3.50}$$

where $\dot{S}_e = \dfrac{\Delta \dot{E}}{\forall}$ . $\Delta \dot{E}$ is calculated from Equation (3.45). $h$ and $\lambda$ are the static enthalpy and the thermal conductivity of the gas, respectively.

### 3.4    Droplet Dispersion Model

The dispersion of the droplet, due to turbulence, is modeled using the method of Gosman and Ioannides.[18] In this method, an instantaneous gas velocity is used in the droplet equations of motion. The instantaneous gas velocity is evaluated from the time-averaged gas velocity, the turbulent kinetic energy, and dissipation rates. For this purpose, the turbulence is assumed to be isotropic and to possess a Gaussian

29

probability distribution function in the fluctuating velocity, whose standard derivation is given by

$$\sigma = \left(\frac{2k}{3}\right)^{1/2}$$

(3.51)

where $k$ is the turbulence kinetic energy in the computational cell, where the droplet is located. Random sampling of this distribution at appropriate times intervals along the droplet trajectory yields the fluctuating velocity of the gas and hence the instantaneous gas velocity.

The sampled fluctuating velocity is applied over a time interval called the interaction time, in the droplet trajectory calculation. The interaction time can be thought of as the time scale, associated with a turbulent eddy. There are two possible events: (a) the droplet moves sufficiently slowly relative to the gas to remain within the eddy during its lifetime ($t_e$); (b) the relative velocity between the droplet and gas is sufficient to allow it to traverse the eddy in a transit time ($t_r$). The interaction time scale will be the minimum of the time scales in the above events, i.e.,

$$t_{int} = min \ (t_e, \ t_r)$$

(3.52)

The eddy and transit time scales can be estimated as follows.

The eddy characteristic length scale is assumed to be the dissipation length scale,

$$\ell_e = C_\mu^{1/2} \frac{k^{3/2}}{\varepsilon}$$

(3.53)

where $\varepsilon$ is the turbulence dissipation rate.

The eddy lifetime is then estimated as:

30

$$t_e = \frac{\ell_e}{|u'|} \tag{3.54}$$

The transit time scale, $t_r$, is estimated from the following solution of a simplified and linearized form of the equations of motion of the droplet

$$t_r = -\tau \, ln\left[1.0 - \left(\frac{\ell_e}{\tau |\mathbf{U} - \mathbf{v}|}\right)\right] \tag{3.55}$$

where $\tau$ is the droplet relaxation time given by

$$\tau = \frac{4}{3} \rho_d \frac{d}{(\rho \, C_D |\mathbf{U} - \mathbf{v}|)} \tag{3.56}$$

In the case when $\left(\frac{\ell_e}{\tau |\mathbf{U} - \mathbf{v}|}\right) > 1$ , the above equation has no solution. This implies that the droplet is captured by the eddy, in which case $t_{int} = t_e$.

## 3.5    Linear Stability Model for Impinging Jet Atomization

A preliminary stability analysis was conducted to determine the sizes of the droplets that would result from the impact of the liquid jets. Daniel Wiehs[21] has obtained the following expression for the stability of a radially moving liquid sheet in stagnant air:

$$w = \frac{vk^2 (\rho_L H)^{1/2}}{2}\left[-1 + \left(1 + \frac{8(\rho_G k U^2 - \sigma k^2)}{v^2 k^4 \rho_L H}\right)^{1/2}\right]$$

$$\tag{3.58}$$

where

$$w \quad = \quad \text{growth rate of the surface wave}$$

31

$\nu$ = kinetic viscosity of liquid

$\rho_L$ = liquid density

$\rho_G$ = gas density

$H$ = liquid sheet thickness

$U$ = sheet velocity

$\sigma$ = surface tension

$k$ = wave number ($m^{-1}$)

The liquid density is estimated as an average of the densities of MMH and NTO. The liquid velocity is calculated from the mass flow rate of MMH and the cross-sectional inlet area. The initial thickness of the sheet (H) is taken to be twice the size of the MMH inlet. This expression is valid only for the low speed breakup of the sheet, *i.e.*, drop sizes are of the order of the sheet thickness. Figure 3-2 shows the variation of growth rate with wavenumber.
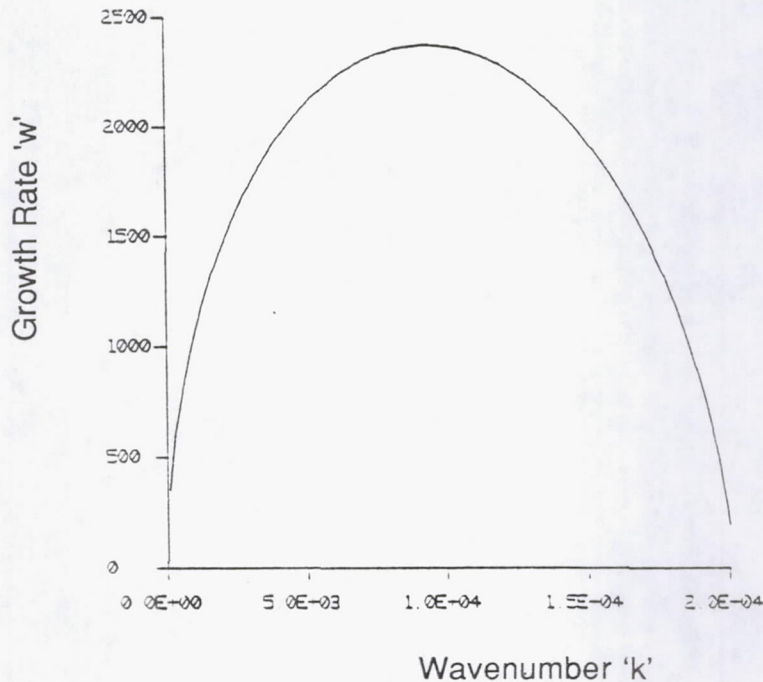


Figure 3-2. Plot of Growth Rate Versus Wave Number

4075/3

However, the above analysis assumes that the gas or the ambient is stationary. This is not the case inside the VTE chamber, where strong recirculation zones (resulting from the geometry of the chamber) can result in droplets being stripped away from the surface of the liquid sheet. The drop sizes resulting from the high speed breakup are considerably smaller. The low speed analysis for this problem predicts a maximum drop size of about 300 microns. A mean drop size of 50 microns is used in the calculations in order to approximately account for high speed atomization phenomena. A lognormal distribution (about the mean size) is used to calculate other drop sizes.

4075/3

## 4.    MODEL VALIDATION

### 4.1    Radiation Model

The discrete-ordinate radiation model, implemented in the present code, has been validated with several benchmark cases, for which exact analytical solutions are available. First, the radiative heat transfer in a square enclosure with an absorbing medium is considered. The walls of the enclosure are maintained at 0°K and the gas in the enclosure is maintained at 500°K. Results are obtained for various optical thickness. A 10 X 10 grid and the S4 approximation, *i.e.* 12 ordinate sets, are used for all these cases. Figures 4-1a through 4-1c show the non-dimensional radiative heat transfer at the cold walls for three optical thicknesses of 0.1, 1.0, and 10.0. The circles represent the numerical solution and the lines show the exact analytical solution reported in Lockwood and Shah (1981). As can be seen, the agreement is very good.

Next, the radiative heat transfer in a square enclosure with a strongly participating medium is considered. In this problem, the east, west and north walls are maintained at 0°K and the south wall is maintained at 1000°K. All the walls are black and the gas scattering coefficient is zero. Figures 4-2a through 4-2c show the radiation heat transfer at the south wall for absorption cross-sections of 2.0, 1.0, and 0.1 respectively. A 21 X 21 grid and the S4 discrete-ordinate approximation are used for these calculations. The open symbols show the exact solution reported by Razzaque *et al.* (1983), and the lines show present predictions. Again, the model results show good agreement with the exact solution.

Finally, radiative heat transfer for pure scattering in a square grey enclosure is considered. This case is quite important, because the boundary conditions are not only a function of the surface emissive power but also of the incident radiant energy. The boundary conditions for this case are the same as in the previous case. A 25 X 25 uniform grid system is used for this case. Figures 4-3a through 4-3c show the surface heat transfer at the hot wall for wall emissivities of 1.0, 0.5, and 0.1 respectively. The comparison with exact solutions are quite good, except for the low surface emissivity case. For this case, the error in the intensity calculation affects the boundary condition to a large extent. The results can be improved by refining the grid and increasing the number of ordinate sets considered.
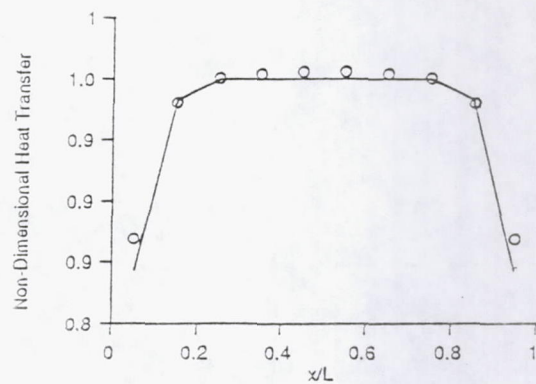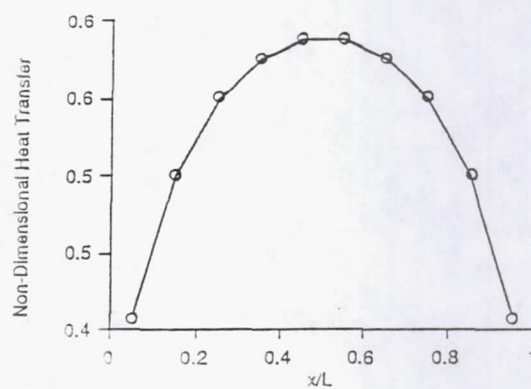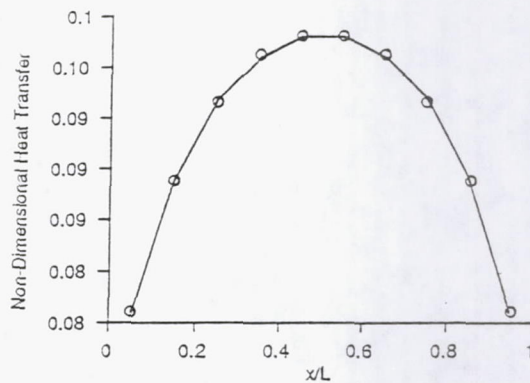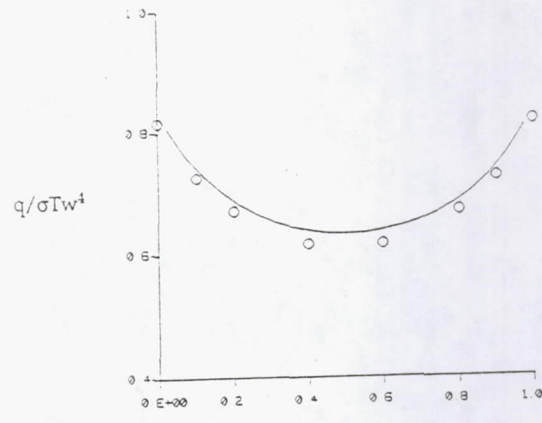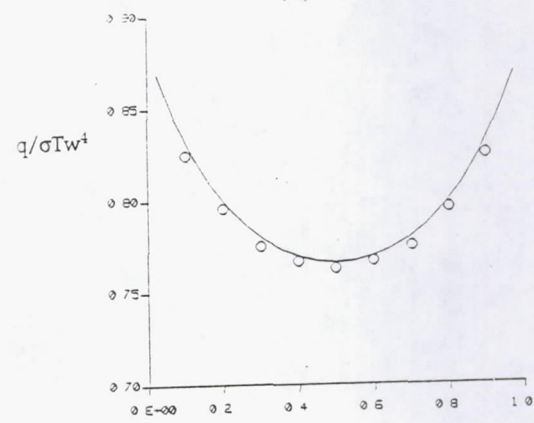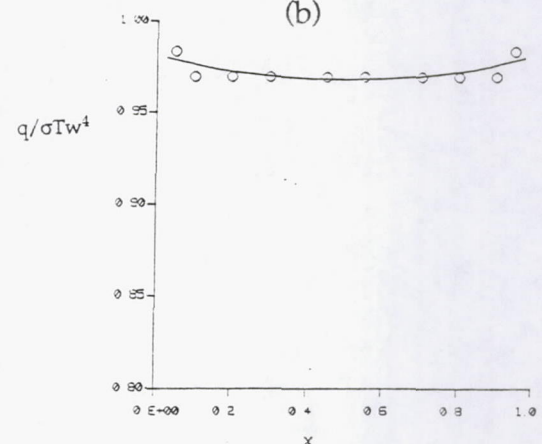
Figure 4-1. Surface Heat Transfer Rates for a Square Enclosure with Cold Black Walls and an Absorbing Medium for Various Optical Thicknesses: (a) 0.1, (b) 1.0 and (c) 10.0. o, - numerical simulation; ---, exact solution from Lockwood and Shah.[14]
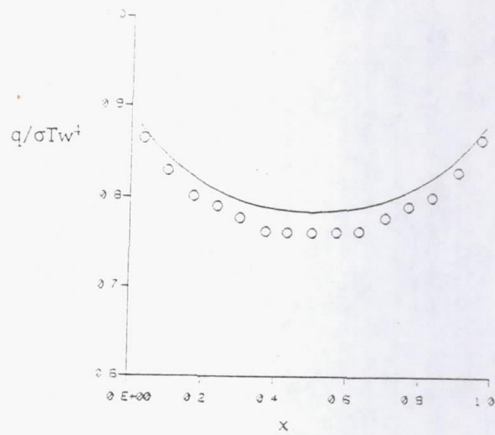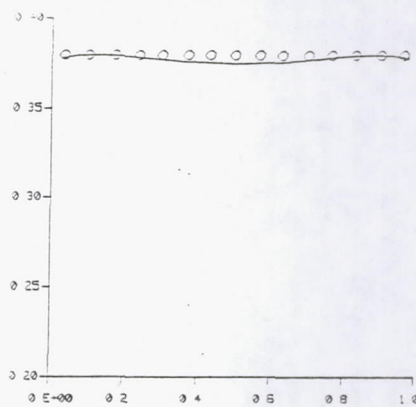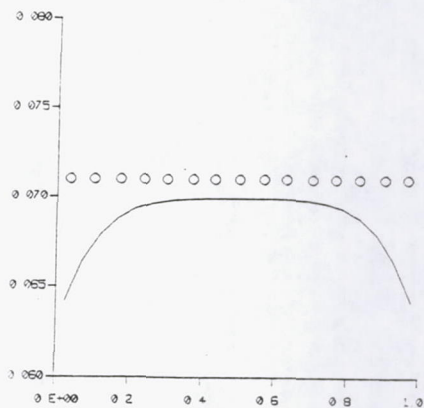
35

Figure 4-2. Radiative Heat Transfer at the Hot Wall of the Square Enclosure Problem for Various Absorption Cross-Sections: (a) 2.0; (b) 1.0; and (c) 0.1. o, - exact solution[15]; ---, present prediction

Figure 4-3.   Radiative Heat Transfer at the Hot Wall of the Square Enclosure
Problem with Grey Walls and Pure Scattering Medium for Various
Wall Emissivities:  (a) 1.0; (b) 0.5; and (c) 0.1.  o, - exact solution[15];
----, present prediction

37

## 4.2    Chemical Equilibrium Model

The objective of this analysis was to use the chemical equilibrium model to predict species distributions in the SSME combustor/nozzle and to compare the predictions with the TDK[22] program (TDE option).  Figure 4-4 shows the grid (385 x 50) for the SSME combustor/nozzle.  The boundary conditions for the problem are:

a.    Inlet:
      u = 320.5 m/s
      p = 19.8 MPa
      T = 3585°K
      Composition:        91.1% $H_2O$, 4.4% OH, 3.5% $H_2$, 0.56% $O_2$, 0.25% O, 0.19% H

Figures 4-5a and 4-5b show the temperature distribution predicted by the TDE and the REFLEQS codes.  It is observed that the REFLEQS predictions match well with the TDE solution.  Figures 4-6a, 4-6b and 4-6c show the distribution of species ($H_2$, $O_2$, and $H_2O$, respectively) along the nozzle centerline.  The symbols are the results of the TDE program.  It is observed that the chemical equilibrium model in REFLEQS predicts correctly the variation in concentration of the above species in the nozzle.
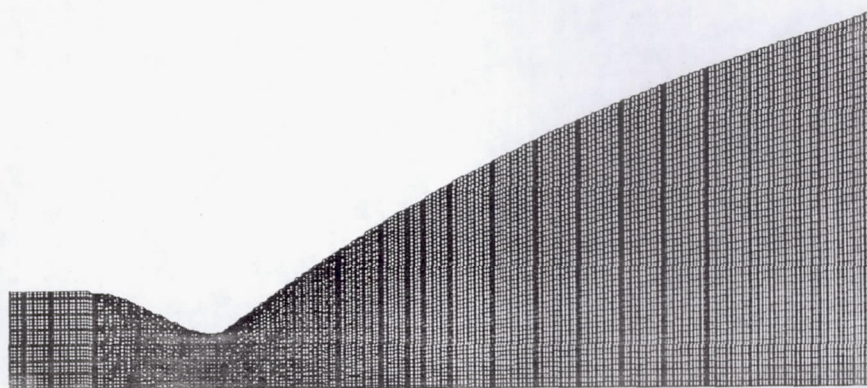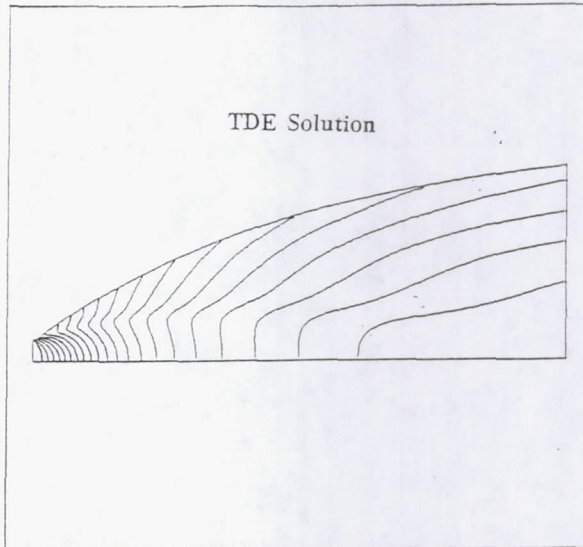


Figure 4-4.  Computational Grid for the SSME Nozzle (385x50)

```
TEMP   CONTOURS
FMIN  7 984E+02
FMAX  6 073E+03
UNITS (DEG-R)
CONTOUR LEVELS
 1     1 813E+03
 2     2 026E+03
 3     2 239E+03
 4     2 452E+03
 5     2 665E+03
 6     2 878E+03
 7     3 091E+03
 8     3 304E+03
 9     3 517E+03
10     3 730E+03
11     3 943E+03
12     4 156E+03
13     4 369E+03
14     4 582E+03
15     4 795E+03
16     5 008E+03
17     5 221E+03
18     5 434E+03
20     5 860E+03
```

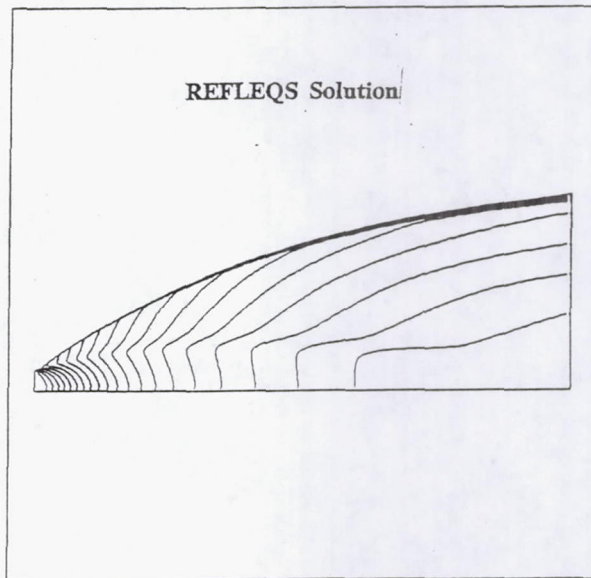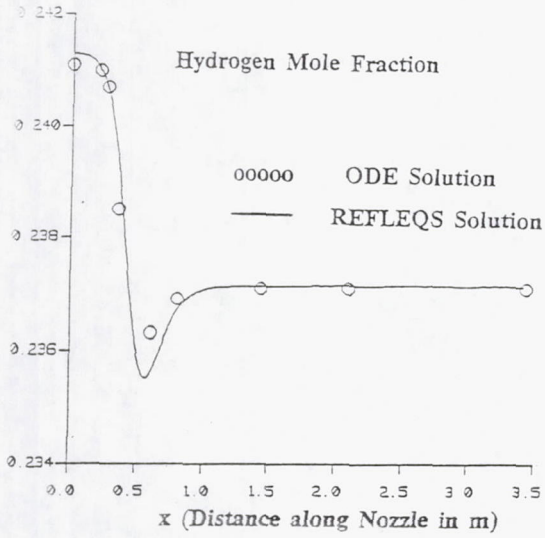TDE Solution

(a)

```
XY PLANE  1
TEMP   CONTOURS
FMIN  7 728E+02
FMAX  3 435E+03
CONTOUR LEVELS
 1     1 007E+03
 2     1 125E+03
 3     1 244E+03
 4     1 362E+03
 5     1 480E+03
 6     1 599E+03
 7     1 717E+03
 8     1 836E+03
 9     1 954E+03
10     2 072E+03
11     2 191E+03
12     2 309E+03
13     2 427E+03
14     2 546E+03
15     2 664E+03
20     3 256E+03
OK>
```
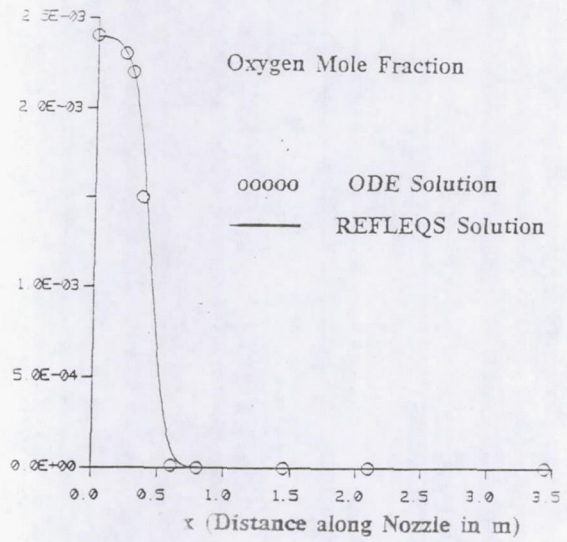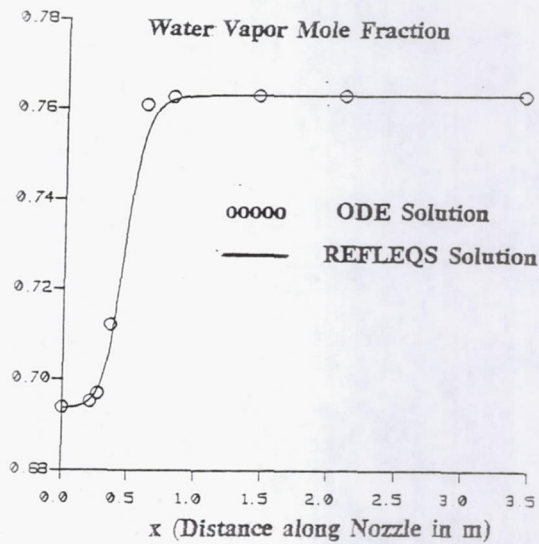
REFLEQS Solution

(b)

Figure 4-5.  Temperature Distribution in the Nozzle

39

Figure 4-6. Species Distribution in the Nozzle

## 5. COMPUTATIONAL RESULTS

In this section, the computational results of VTE performance obtained using the REFLEQS code are presented. A number of simulations were performed to assess the effects of various physical phenomena occurring in the thrust chamber of the VTE. These effects are discussed separately in several sections.

The first section (5.1) discusses the performance of VTE obtained using the gas-gas combustion model. The VTE performance is analyzed for three power levels, namely 100%, 50%, 10%. An equilibrium chemistry model with 13 species is used for all the cases.

The second section (5.2) considers the effect of atomization and spray. Calculations for the three power levels are obtained using a mean drop size of 50 microns with a lognormal distribution of sizes ranging from 25-100 microns. A parametric study on the effect of drop sizes is also included in this section. An equilibrium chemistry model is used for these cases. The spray model used in obtaining these results is described in Section 3.3

The third section (5.3) presents the effect of radiation on the performance and wall cooling requirements of VTE. The $S_4$ approximation (12 ordinate directions) of the discrete ordinate radiation model is used for obtaining these results. The temperature distributions in VTE chamber/nozzle with and without invoking the radiation model are compared.

Finally, in Section 5.4, the effect of the radiation heat shield on heat transfer characteristics is discussed. The heat shield is designed to protect the structure surrounding the engine from the radiation. For all these calculations, a solution is regard to be converged when the residuals of all the variables have dropped by 5 orders of magnitude.

### 5.1    Gas-Gas Combustion Model

In the Gas-Gas combustion model, it is assumed that atomization and vaporization occurs instantaneously at the injection location. In reality atomization and

41

vaporization occur during a finite time scale. But the Gas-Gas model will be useful in providing an understanding of the flow and combustion processes occurring inside the VTE thrust chamber. For all the VTE performance calculations, an equilibrium chemistry model was used to simulate combustion. In the previous phase of this study, instantaneous and finite rate chemistry models with five species (MMH, NTO, $CO_2$, $H_2O$, and $N_2$) were considered for the reaction between MMH and NTO. The ODE analysis for this system, however, shows that many more species are involved in this reaction which needs to be considered for accurate prediction of flame temperature. Therefore, a chemical equilibrium model with 13 species was used for the present calculations. A detailed formulation of this model is described in Section 3.1.

### 5.1.1 100% Power Level

For obtaining the following results, the MMH and NTO inlet temperatures are taken to be 300°K. The density of gaseous MMH and NTO are calculated from the specified chamber pressure, and their velocities are calculated from the specified flow rates. The chamber pressure for 100% power level is specified to be 6.89E5 $N/m^2$ (100 psi). For most of the calculations performed, a zero gradient boundary condition for temperature is imposed at the walls. For problems involving radiation, however, a wall temperature distribution is specified. Figure 5-1 shows the Mach number contours in the VTE combustion chamber and nozzle. It is observed that the maximum Mach number at the exit is about 5.0. It is also be observed that the thickness of the boundary layer on the nozzle wall increases with downstream distance. Figures 5-2 and 5-3 show the distribution of temperature and passive scalar concentration of NTO. The maximum temperature in the chamber is seen to be 3300°K which is in good agreement with the calculations of adiabatic flame temperature for this mixture. These results are very similar to the results reported in the previous report[2] indicating that the accuracy of staggered and colocated grid approach are comparable. It should be pointed out, however, that calculations performed during the previous phases of this study[1,2] using instantaneous and finite-rate chemistry models predicted a much higher temperature.

```
MACH   CONTOURS
FMIN   2.162E-03
FMAX   5.049E+00
CONTOUR LEVELS
  2    2.678E-01
  4    7.990E-01
  6    1.330E+00
  8    1.862E+00
 10    2.393E+00
 12    2.924E+00
 14    3.455E+00
 16    3.987E+00
 18    4.518E+00
 20    5.049E+00
```
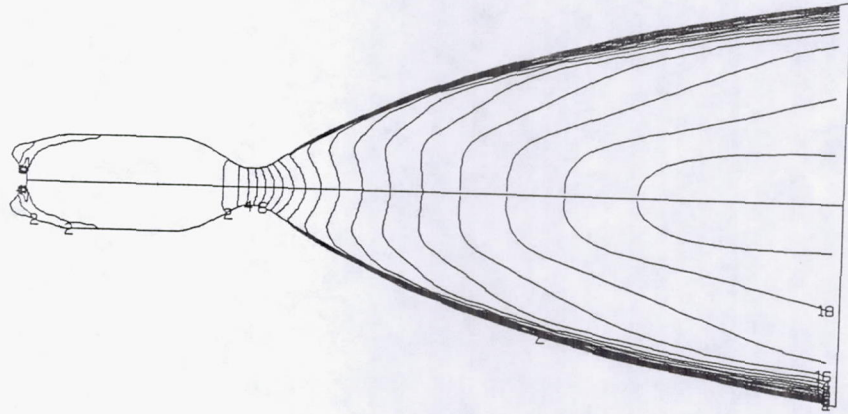
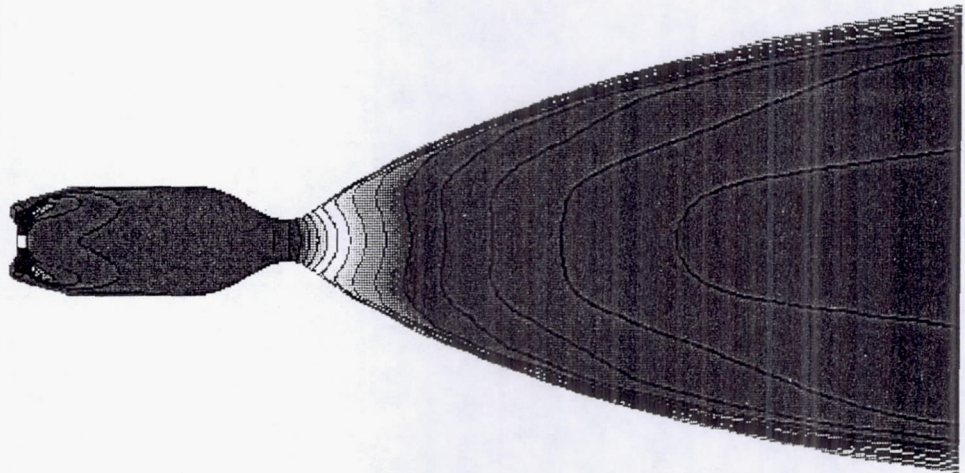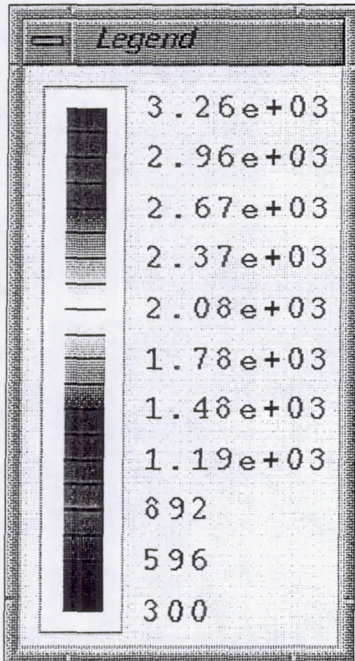Figure 5-1.    Mach Number Distribution in VTE Chamber/Nozzle (Gas-Gas Model, 100% Power Level)



```
Legend
3.26e+03
2.96e+03
2.67e+03
2.37e+03
2.08e+03
1.78e+03
1.48e+03
1.19e+03
 892
 596
 300
```

Figure 5-2.    Temperature Distribution in VTE Chamber/Nozzle (Gas-Gas Model, 100% Power Level)
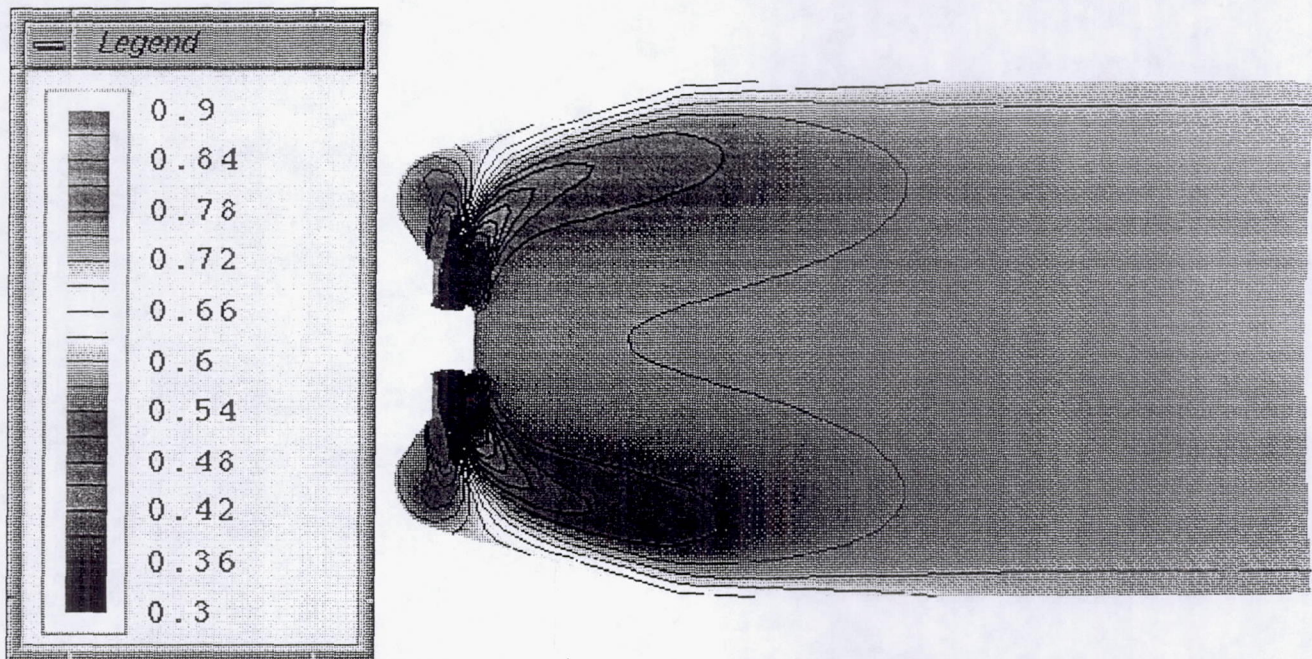
4075/3

Figure 5-3. Passive Scalar Concentration of NTO (Gas-Gas Model, 100% Power Level)

Figure 5-3 indicates that the reaction between MMH and NTO is complete at the location midway between the pintle and the throat. Figure 5-4 shows the velocity vectors inside the combustion chamber. Two recirculation zones are observed, a smaller one in the recessed portion of the chamber dome, and a larger one near the center of the chamber. The presence of this large recirculation zone near the center improves the mixing characteristics in the combustion chamber. As a result, the temperature downstream of the pintle until the throat is nearly uniform. The predicted ISP for this case is about 330 which is about 5% higher than TRW's experimental data. This is to be expected because the gas-gas model does not include the energy required for evaporating the droplets.

```
VELOCITY PLOTS
VELMIN  0.000E+00
VELMAX  1.388E+03
```
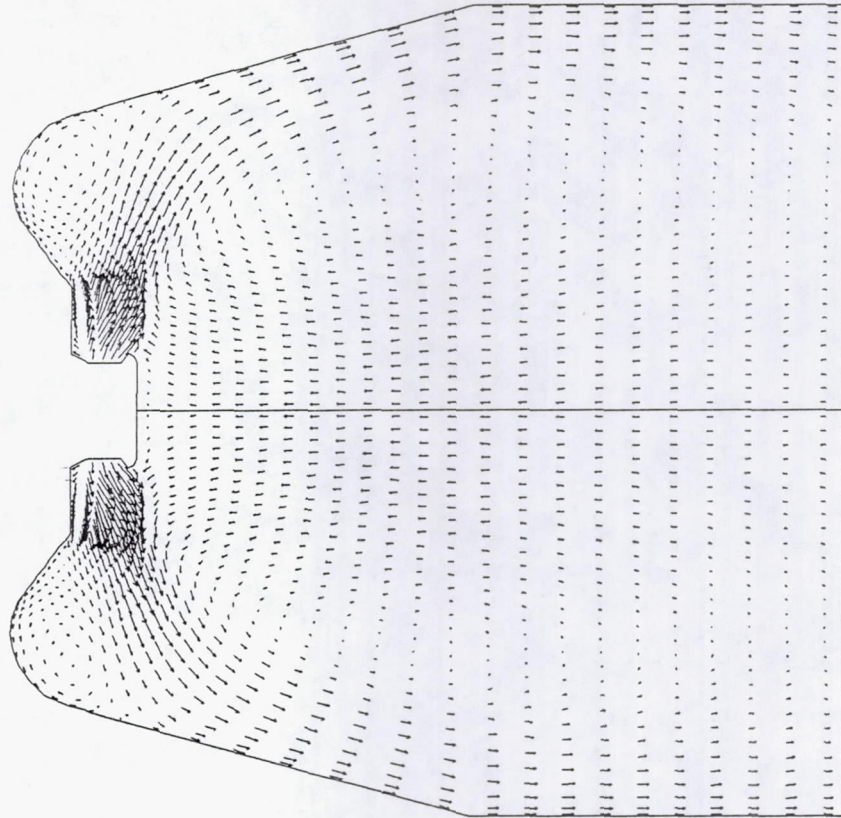
Figure 5-4.   Velocity Vectors in VTE Combustion Chamber (Gas-Gas Model, 100% Power Level)

### 5.1.2   50% Power Level

Next, the performance of VTE at 50% power level is considered.  The chamber pressure for this power level is specified as 3.495E5 $N/m^2$ (50 psi) and the MMH and NTO flow rates are 50% of the full power level.  The inlet area for the incoming gases is assumed to remain constant for all the power levels.  Figures 5-5 and 5-6 show the Mach number and temperature contours for this case.  The maximum Mach number at the exit is very close to the maximum Mach number for the 100% power level.  The maximum temperature in the chamber, however, is about 5% less than the maximum temperature for the 100% power level.  Except for small differences in the magnitudes of Mach number and temperature, the contours for both power level cases are very similar.  Figure 5-7 shows the velocity vectors in the

45

combustion chamber. Again, the velocity vectors for both power level cases are very similar except that the recirculation zones are weaker in this case due to reduced mass flow rates. The ISP predicted for this case is slightly smaller than that for the previous case mainly due to the off-design conditions.

```
MACH   CONTOURS
FMIN   2.442E-03
FMAX   4.921E+00
CONTOUR LEVELS
  2     2.613E-01
  4     7.790E-01
  6     1.297E+00
  8     1.814E+00
 10     2.332E+00
 12     2.850E+00
 14     3.368E+00
 16     3.885E+00
 18     4.403E+00
 20     4.921E+00
```
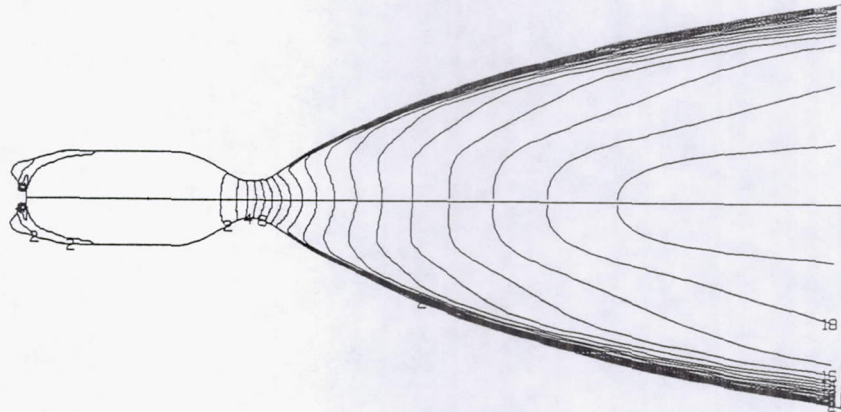
Figure 5-5. Mach Number Distribution (Gas-Gas Model, 50% Power Level)

Legend

```
3.18e+03
2.9e+03
2.61e+03
2.32e+03
2.03e+03
1.74e+03
1.45e+03
1.17e+03
877
588
300
```
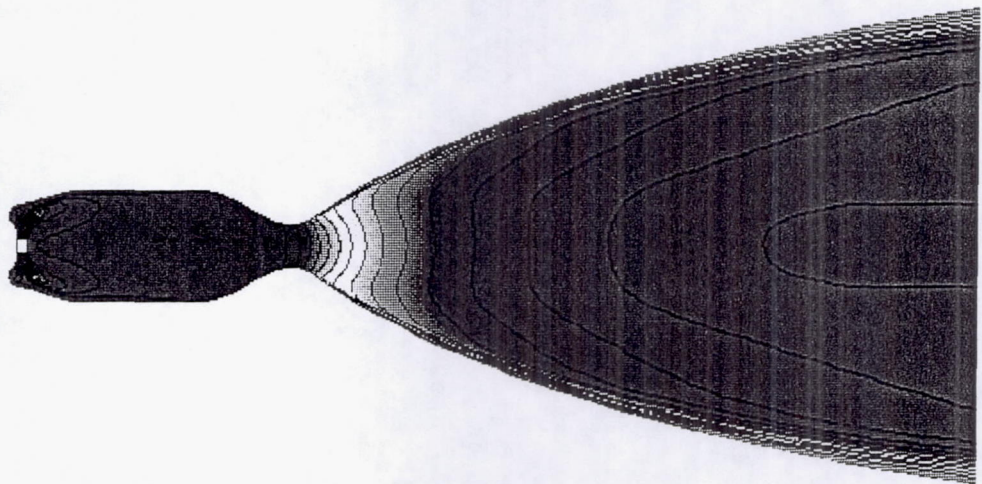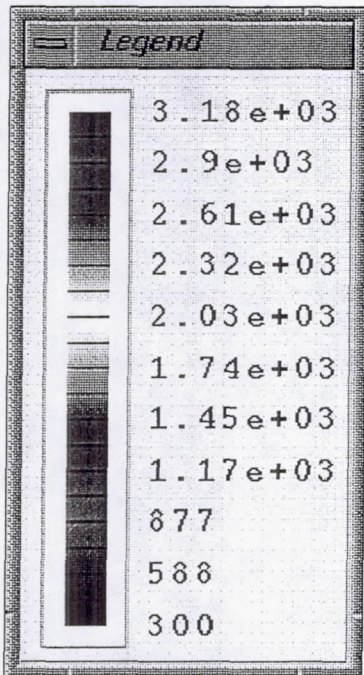
Figure 5-6. Temperature Distribution (Gas-Gas Model, 50% Power Level)

```
VELOCITY PLOTS
VELMIN   0.000E+00
VELMAX   1.372E+03
```
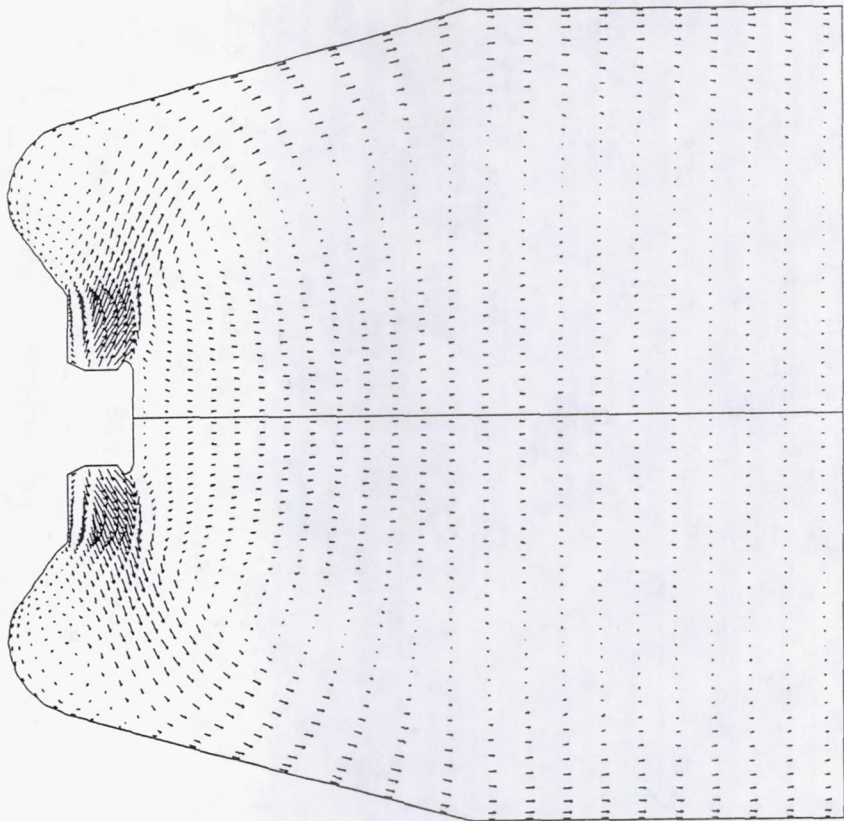
Figure 5-7. Velocity Vector Plot (Gas-Gas Model, 50% Power Level)

### 5.1.3  10% Power Level

The Mach number and temperature contours for the 10% power level are shown in Figures 5-8 and 5-9. The chamber pressure for this case is 10 psi. The propellant flow rates are reduced to 1/10th of the flow rate at full power level. For the 10% power level, the maximum Mach number at the exit is about 4.6 which is 8% less than that for the full power level case. The maximum temperature in the combustion chamber is 3000°K which is 200°K less than the maximum temperature at full power level. Figure 5-10 shows the velocity vectors in the combustion chamber. It can be observed that the recirculation zone above the pintle has almost disappeared because of the lower velocity of the gases and the recirculation zone at the center is very weak. The ISP predicted at this power level is 325. This is slightly less when compared to the ISPs at other power levels mainly due to reduced efficiency at this condition. The following section presents the results obtained using the spray model.

47

```
MACH   CONTOURS
FMIN   3.019E-03
FMAX   4.627E+00
CONTOUR LEVELS
  2    2.464E-01
  4    7.331E-01
  6    1.220E+00
  8    1.707E+00
 10    2.193E+00
 12    2.680E+00
 14    3.167E+00
 16    3.654E+00
 18    4.140E+00
 20    4.627E+00
```
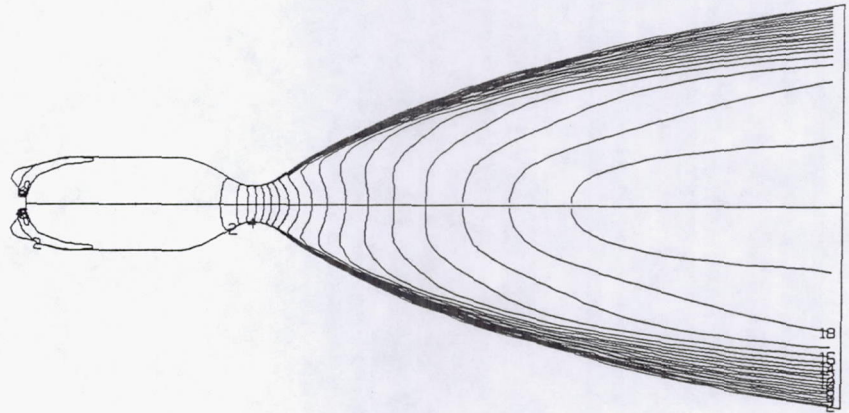
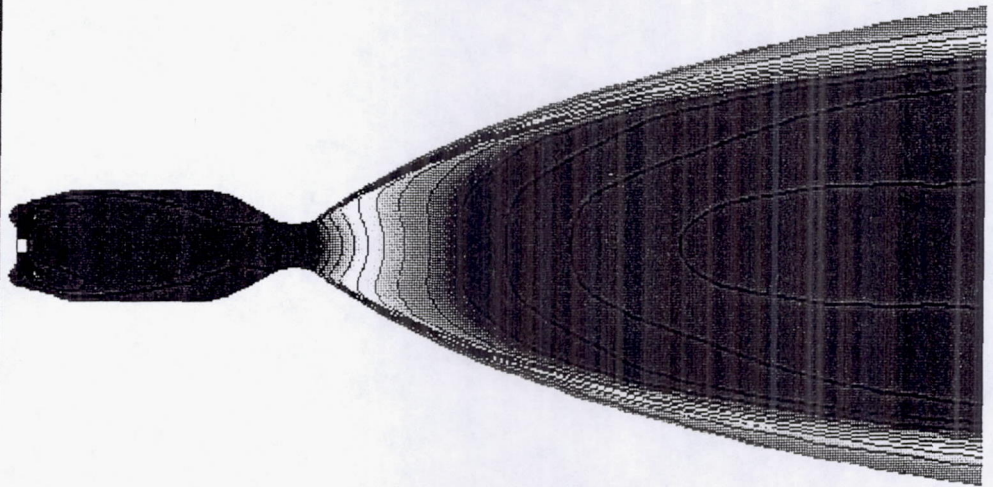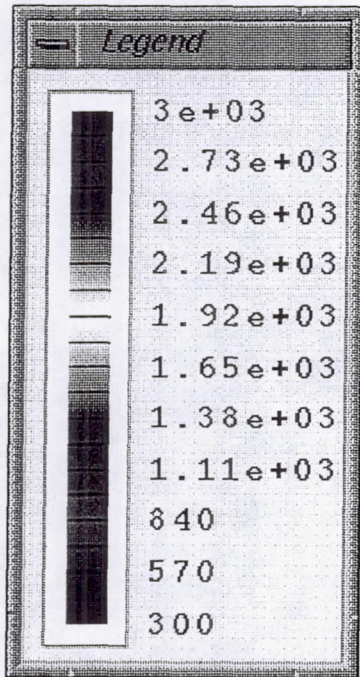Figure 5-8.  Mach Number Distribution (Gas-Gas Model, 10% Power Level)



```
Legend

3e+03
2.73e+03
2.46e+03
2.19e+03
1.92e+03
1.65e+03
1.38e+03
1.11e+03
840
570
300
```

Figure 5-9.  Temperature Distribution (Gas-Gas Model, 10% Power Level)

48

```
VELOCITY PLOTS
VELMIN  0.000E+00
VELMAX  1.361E+03
```
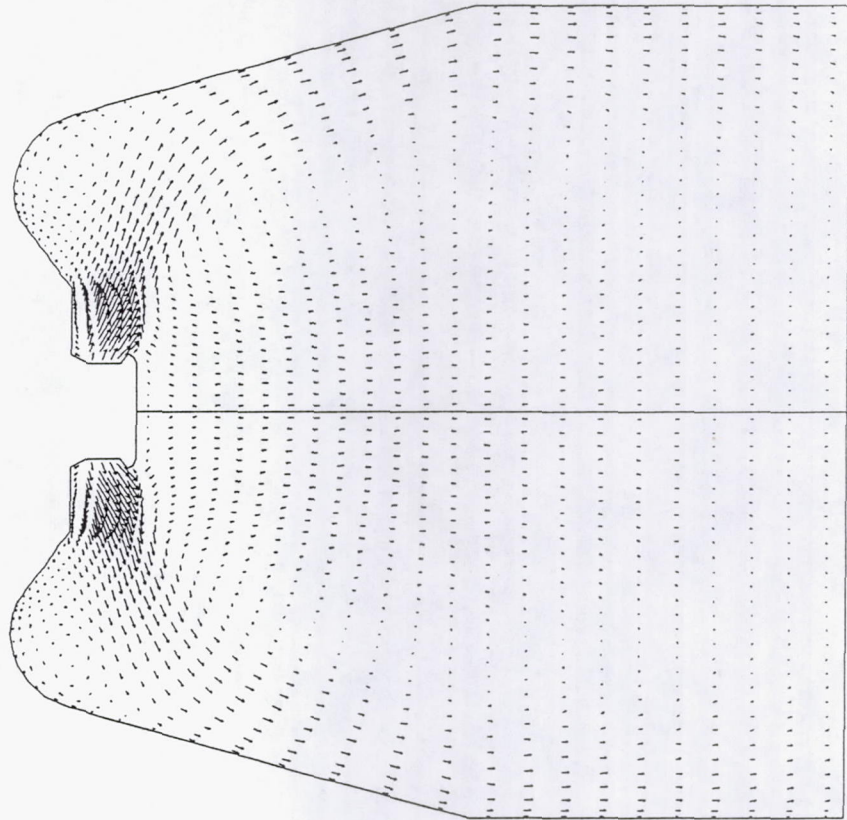
Figure 5-10.  Velocity Vector Plot (Gas-Gas Model, 10% Power Level)

## 5.2    Liquid-Gas (Spray) Combustion Model

In this section, the performance of VTE predicted by the spray model is discussed. The spray model incorporated in the REFLEQS code is based on the Eulerian-Lagrangian methodology of two-phase flows discussed in Section 3.3. For accurate prediction of performance, a good estimate of the droplet initial conditions are required. The linear stability analysis of impinging jets, discussed in Section 3.5, predict a maximum drop size of 300 microns for MMH and NTO liquid jets. This analysis is strictly valid for low speed atomization and jets exhausting into still ambience. However, in the VTE combustion chamber, the liquid fan formed by the impingement of MMH and NTO is surrounded by recirculating and chemically reacting gaseous mixture. The breakup process in this situation is expected to be due to the high speed atomization mechanism for which the droplet size would very small. Also, the secondary atomization process would make the droplet size still

49

smaller. Due to these reasons, the droplet sizes produced by the VTE pintle injector are expected to be significantly less than that predicted by the linear stability analysis.

For the following simulations, a log-normal drop size distribution is specified with a mean droplet size (SMD) of 50 microns. The droplet sizes are selected in the 25 to 100 microns range to fit a log-normal curve with a standard deviation of 0.2. Figure 5-11 shows the liquid mass fraction as a function of drop size. A parametric study is performed to understand sensitivity of predictions to initial drop size distribution.

### 5.2.1 100% Power Level

Figure 5-12 shows the trajectories of droplets for the 100% power level conditions. All the drops are released at the point of impact of the two jets. The initial droplet velocity is expected to be an average of liquid sheet velocity and gas velocity near the interface. In the previous report[2], a parametric study on initial droplet velocities was performed. That study showed that the mixing in the combustion chamber depends on the magnitude of the droplet velocity. Higher droplet velocities lead to smaller residence times and sufficient mixing is not achieved. On the other hand, smaller droplet velocities gives rise to a well mixed zone in the central region of the combustor. Based on the results of that study, a mean droplet velocity of 35 m/sec is used for all the power level cases with a 5% random variation in velocity is specified for each droplet size group. The trajectory plot indicates that the penetration of smaller droplets is significantly less than the penetration of larger droplets. It is clear that larger droplets impinge on the combustion wall and slide along the wall before they evaporate. It is also clear that the spray is very dense near the injection point. Figures 5-13 and 5-14 show the Mach number and temperature contours for this case. The maximum Mach number at the exit is 4.8 which is slightly less than the prediction of gas-gas model. The temperature contours show that there are large temperature gradients in the combustion chamber due to the presence of relatively cold droplets. In the predictions of gas-gas model, the temperature in the chamber was nearly uniform. The hottest zone is in the center of the combustion chamber. As a consequence, the head end of the pintle is expected to be very hot. This has been proven in the VTE hot fire tests. Later designs of VTE use an ablative material cast on the front end of the pintle injector.
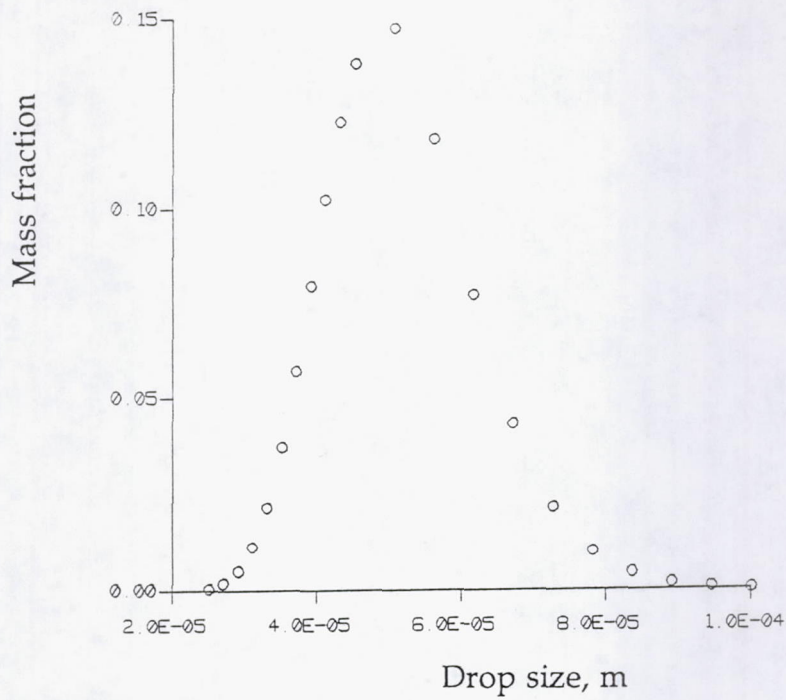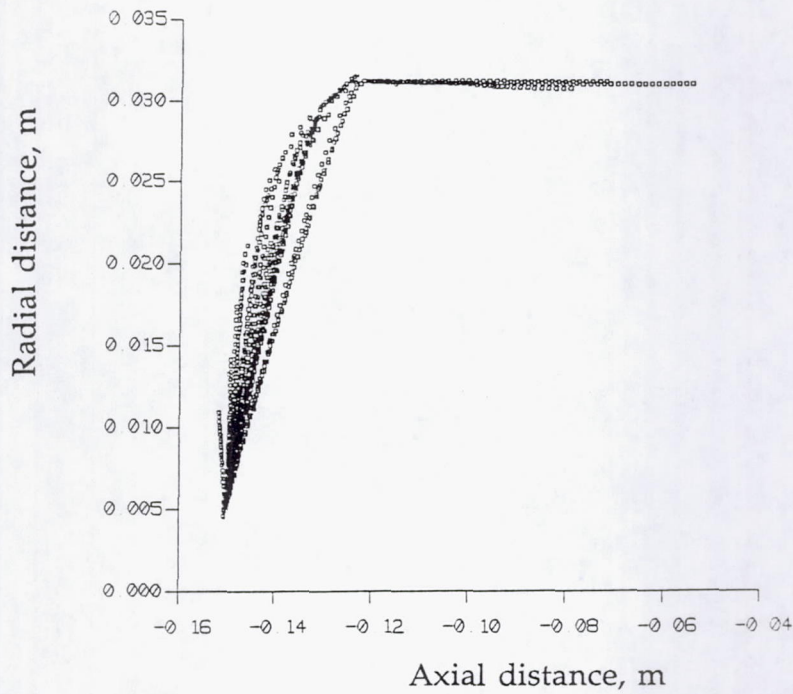
Figure 5-11. Lognormal Drop Size Distribution for 50μ SMD



Figure 5-12. Droplet Trajectory Plot (Spray Model, 100% Power Level)

51

```
MACH   CONTOURS
FMIN   3.139E-04
FMAX   4.786E+00
CONTOUR LEVELS
  2    2.522E-01
  4    7.559E-01
  6    1.260E+00
  8    1.763E+00
 10    2.267E+00
 12    2.771E+00
 14    3.275E+00
 16    3.778E+00
 18    4.282E+00
 20    4.786E+00
```
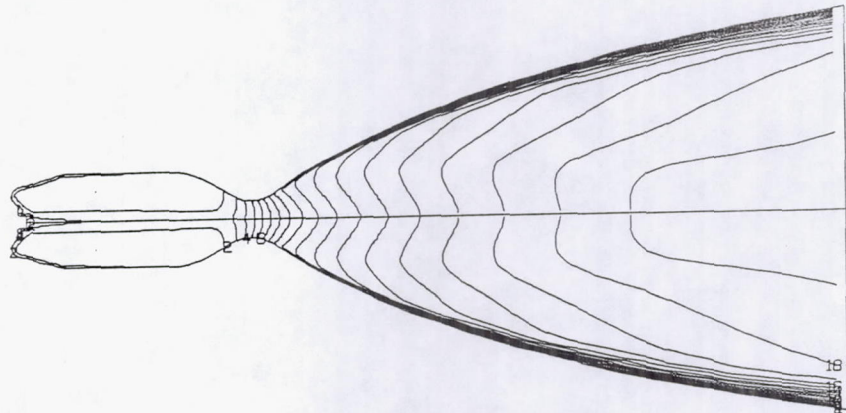
Figure 5-13.  Mach Number Distribution in VTE Chamber/Nozzle (Spray Model, 100% Power Level)



```
Legend
 3.2e+03
 2.91e+03
 2.62e+03
 2.33e+03
 2.04e+03
 1.75e+03
 1.46e+03
 1.17e+03
  880
  590
  300
```
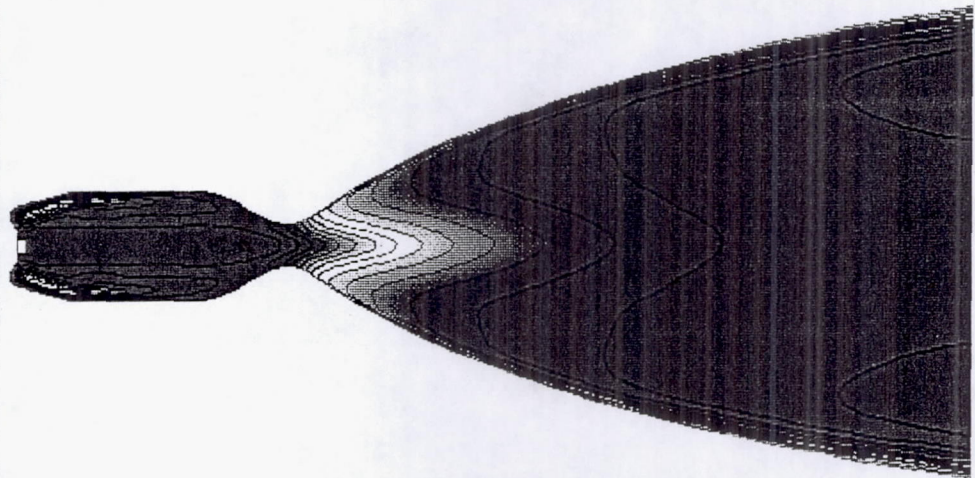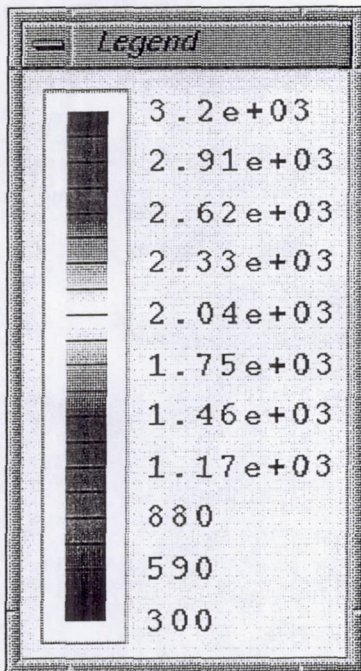
Figure 5-14.  Temperature Distribution (Spray Model, 100% Power Level)

52

Figure 5-15 shows the evaporated mass (kg/sec) of NTO in the combustion chamber. It is clear than even though some of the droplets impinge on the splash plate, most of the evaporation takes place very close to the pintle injector. Figure 5-16 shows the velocity vectors in the chamber for this case. As can be seen, there is no recirculation zone in the swept back region of the combustor dome. The recirculation zone downstream of the pintle is also absent, contrary to the gas-gas model prediction. This is expected because the injection velocity of gas is much higher than the injection velocity of liquid for the same flow rates. The ISP predicted by the spray model is 324 which is slightly less than the ISP predicted by the gas-gas model.
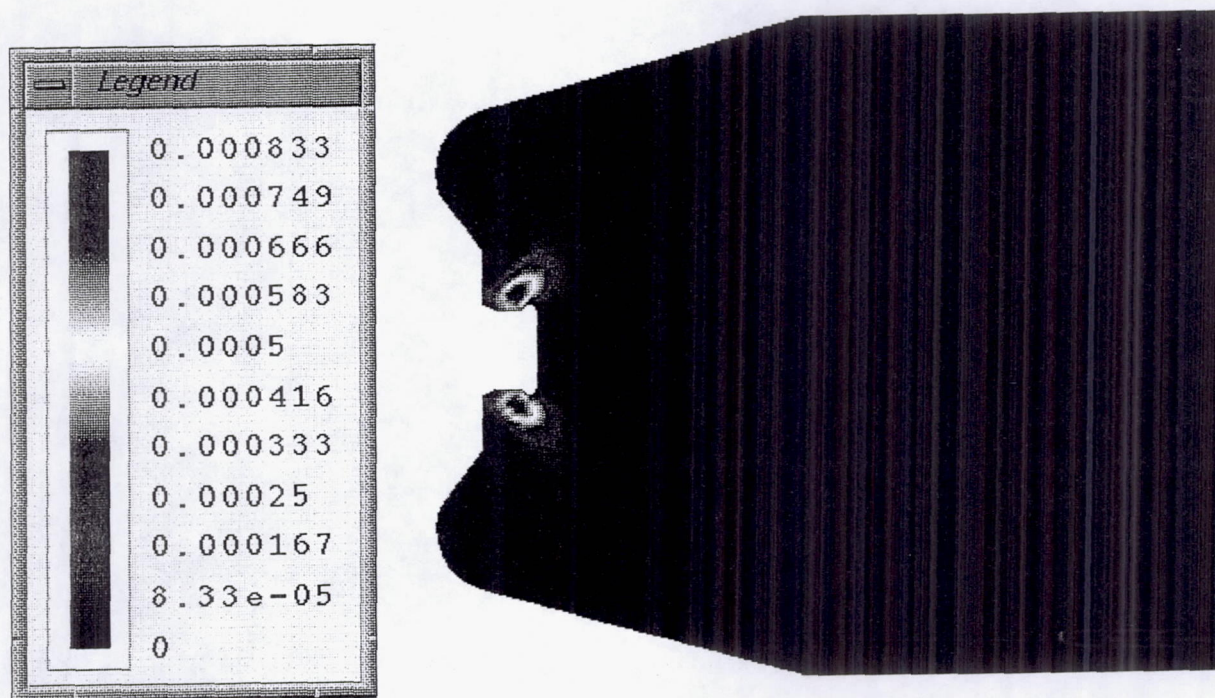


Figure 5-15. Distribution of Evaporated Mass of NTO (Spray Model, 100% Power Level)

4075/3

VELOCITY PLOTS
VELMIN 0.000E+00
VELMAX 9.591E+02
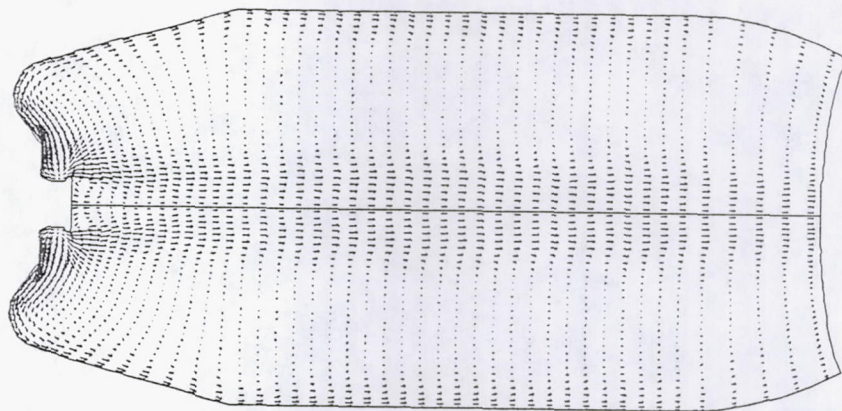
Figure 5-16. Velocity Vectors in VTE Combustion Chamber (Spray Model, 100% Power Level)

### 5.2.2 50% Power Level

Figure 5-17 shows the trajectories of droplets for the 50% power level case. The spreading angle of the spray is slightly more in this case because of the lower chamber pressure. Again the larger droplets do not evaporate before impinging on the wall. Figures 5-18 and 5-19 show the Mach number and temperature contours. Similar to the predictions of the gas-gas model, the maximum Mach number at the exit is slightly lower than that for the 100% power level. The temperature distribution for this case is very similar to the distribution for 100% power level.

4075/3
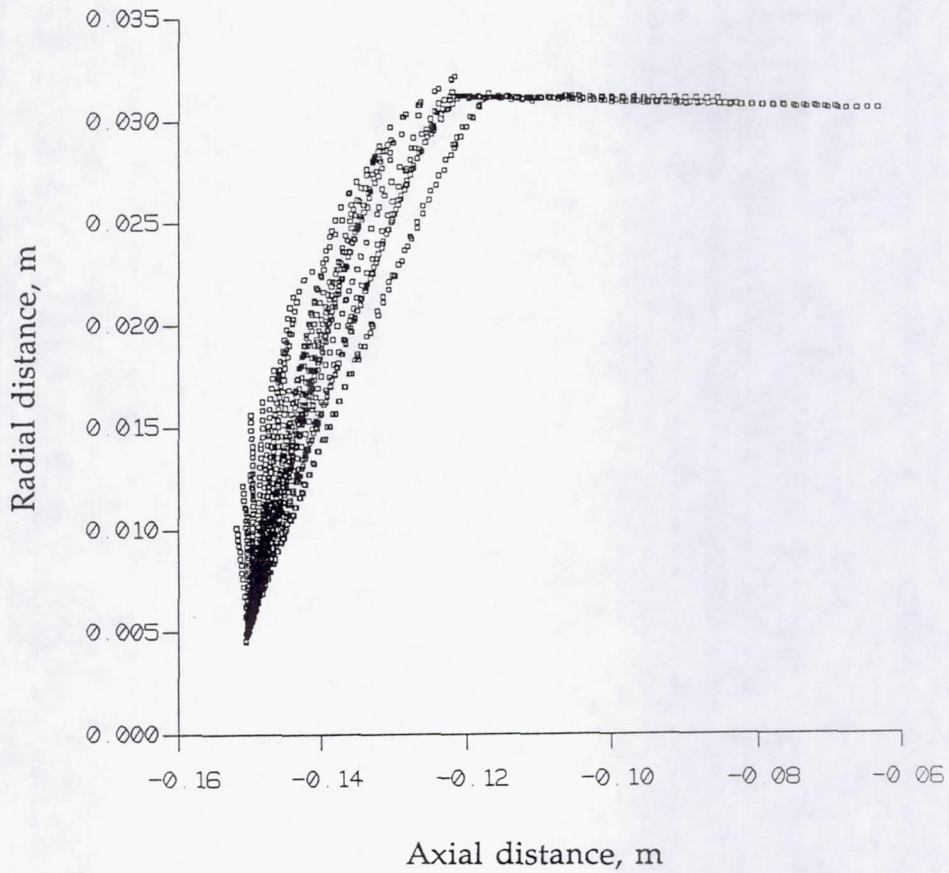
Figure 5-17.  Droplet Trajectory Plot (Spray Model, 50% Power Level)

MACH    CONTOURS
FMIN    4.754E-04
FMAX    4.556E+00
CONTOUR LEVELS
  2     2.402E-01
  4     7.198E-01
  6     1.199E+00
  8     1.679E+00
 10     2.158E+00
 12     2.638E+00
 14     3.117E+00
 16     3.597E+00
 18     4.077E+00
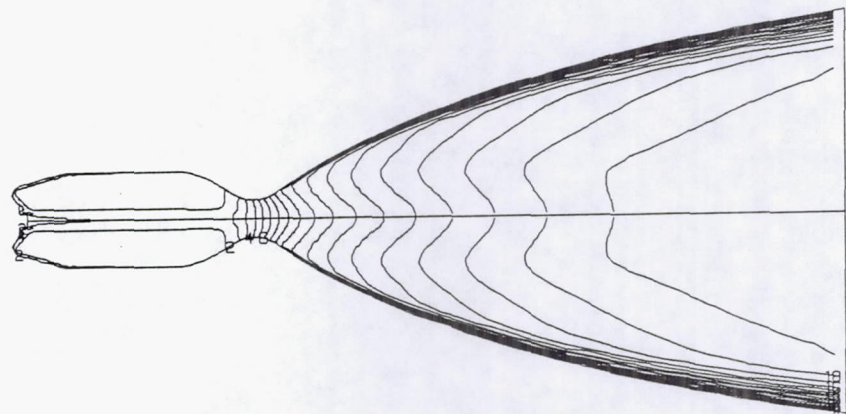 20     4.556E+00



Figure 5-18.  Mach Number Distribution (Spray Model, 50% Power Level)
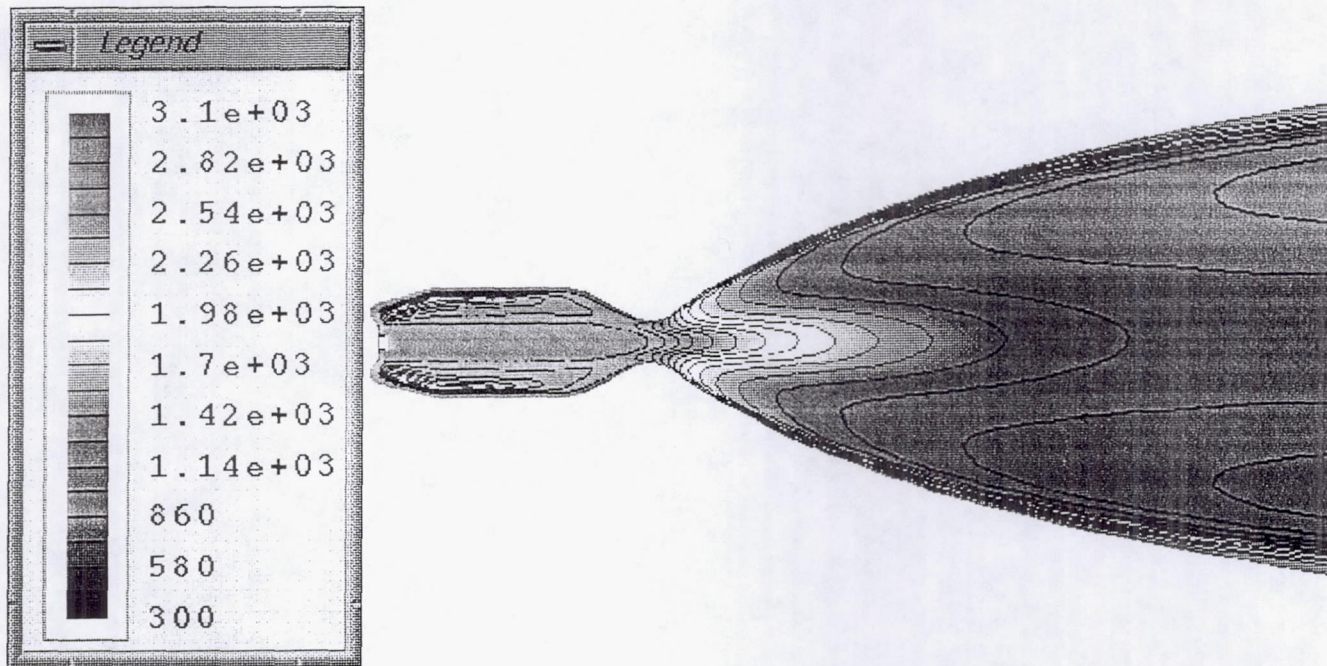
Figure 5-19.  Temperature Distribution (Spray Model, 50% Power Level)

### 5.2.3  10% Power Level

The Mach number and temperature distributions predicted by the spray model for 10% power level are very similar to the corresponding distributions at other power levels.  This is very clear from the Mach number distribution shown in Figure 5-20. As expected, the ISP predicted for this power level is slightly less than that for other power levels.   The next section discusses the effect of droplet sizes on the performance of VTE.

```
MACH   CONTOURS
FMIN   1.007E-02
FMAX   4.954E+00
CONTOUR LEVELS
  2    2.703E-01
  4    7.907E-01
  6    1.311E+00
  8    1.832E+00
 10    2.352E+00
 12    2.873E+00
 14    3.393E+00
·16    3.913E+00
 18    4.434E+00
 20    4.954E+00
```



Figure 5-20.  Mach Number Distribution (Spray Model, 10% Power Level)

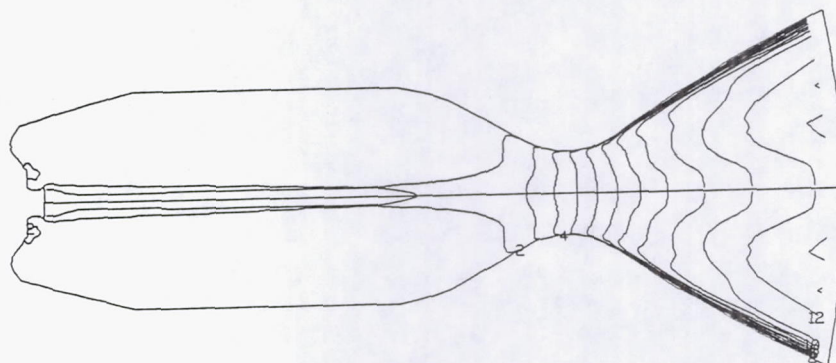56

### 5.2.4  Parametric Variation of Droplet Sizes

The spray model is used to conduct a parametric study to assess the effect of droplet size. Two simulations for mean drop sizes of 25 and 100 microns are performed. Figure 5-21 shows the drop size distributions used in these two cases. Figure 5-22 shows the droplet trajectories for the 25 micron size case. It is observed that droplets evaporate very quickly and very few droplets impinge on the splash plate. The spreading angle of the spray is small compared to the angle for 50 microns size case. Figures 5-23 shows the distribution of evaporated NTO mass. It clearly indicates that evaporation takes place very close to the pintle. Because evaporation takes place quickly, there is sufficient time for mixing and chemical reaction. As a result, the temperature distribution in the combustion chamber is more uniform. Figure 5-24 shows the droplet trajectories for the 100 micron size. As can be seen, more droplets impinge on the combustion wall. The large droplets slide along the combustor wall and evaporate before reaching the throat. Figure 5-25 shows the contours of evaporated NTO mass. Because of the slow evaporation of large drops, combustion takes place until the gases reach the throat region. From these simulations, it is clear that optimum performance can be achieved when the droplet sizes are in the 25-50 microns range.
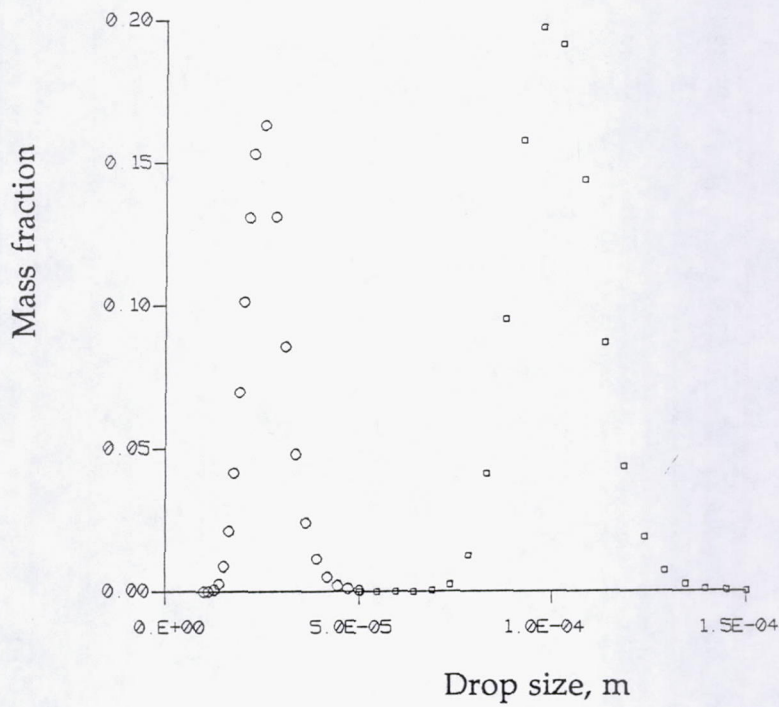
Figure 5-21.  Lognormal Size Distributions for 25µ SMD (o) and 100µ SMD (□)
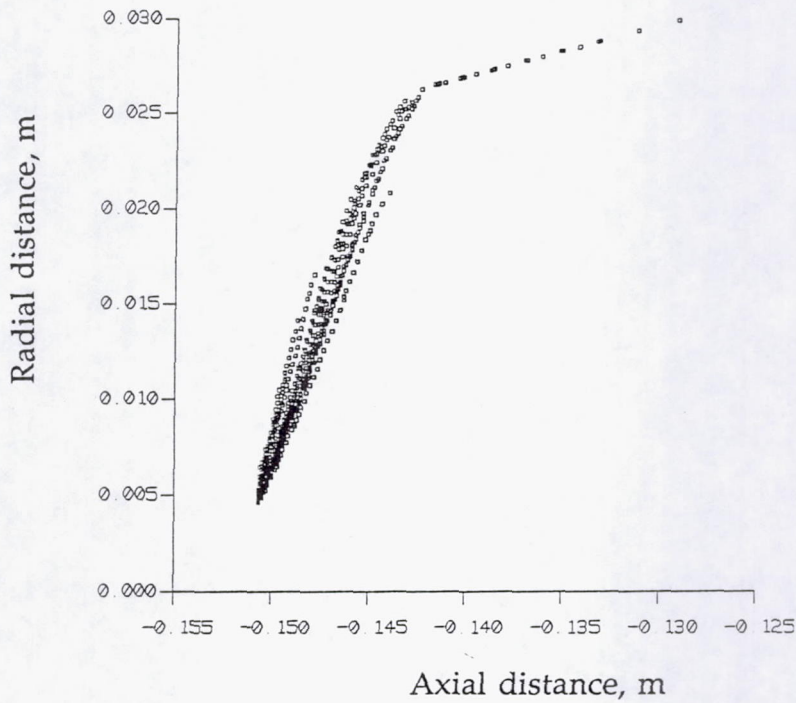


Figure 5-22.  Droplet Trajectories for 25µ SMD (100% Power Level)

58
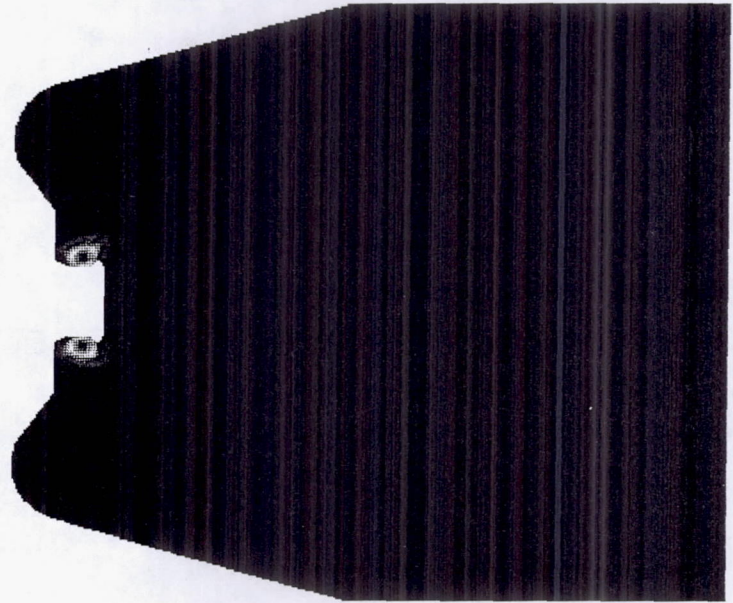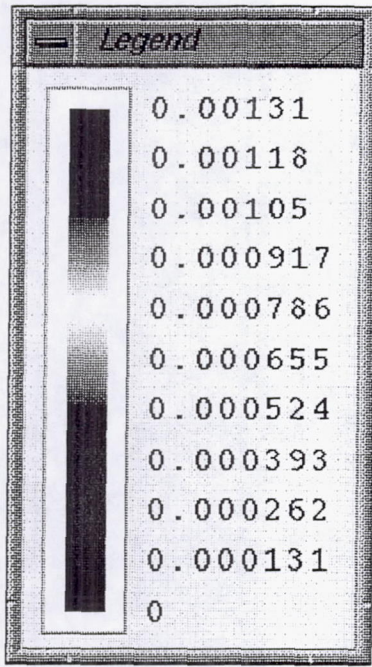
Figure 5-23. NTO Evaporated Mass Distribution for 25 Micron Drop Size (100% Power Level)
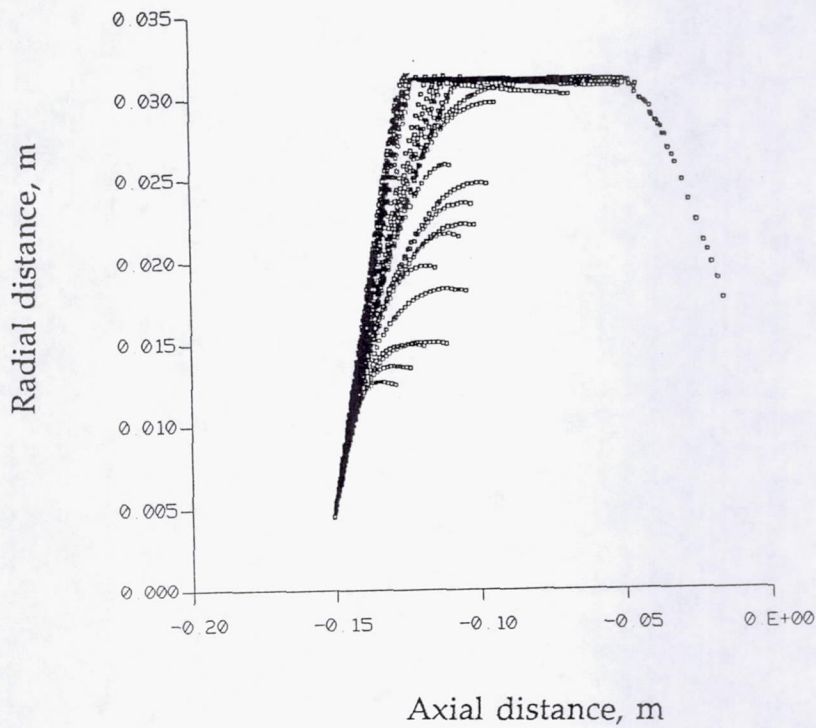


Figure 5-24. Drop Trajectories for 100μ SMD (100% Power Level)
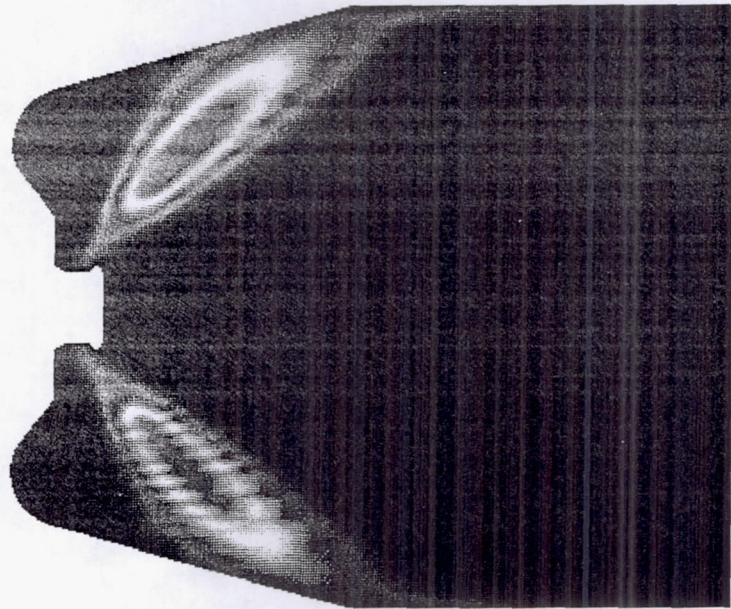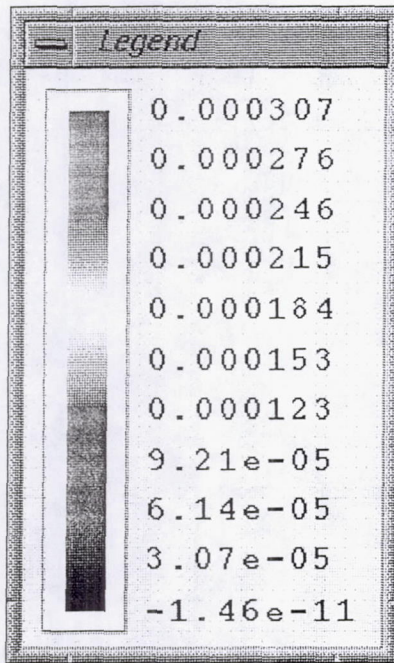
Figure 5-25. NTO Evaporated Mass Distribution for 100 Micron Drop Size (100% Power Level)

## 5.3    Effects of Radiation

In this section, the effect of radiation on flow and heat transfer characteristics in VTE is discussed.  Calculations were performed by invoking the radiation model, using both gas-gas and spray models at 100% power level.  The discrete-ordinate radiation model discussed in Section 2.3 is used with 12 ordinate directions for these simulations.   For accurate prediction of radiative heat transfer, the radiative properties of combustion gases and walls are required.  However, there is a lack of knowledge on the radiative properties (absorptivity and emissivity) of MMH and NTO.  Also, the emissivity and reflectivity of VTE combustor and nozzle walls are not known.  Due to the lack of this information, the radiative properties for a worst case scenario is considered, i.e. the absorptive cross-section of the combustion gas is taken to be unity and the wall emissivity is taken to be unity (black).  Since the wall temperature distribution is not known, the walls are assumed to be maintained at 1000°K.

Figures 5-26 and 5-27 show the temperature distributions predicted using the gas-gas and spray models. Comparing these figures with 5-2 and 5-14 shows that the temperature distribution is not altered by the inclusion of radiation model. This indicates that convective and conductive modes of heat transfer dominate in VTE combustion chamber and nozzle. It is found that the source term for the energy equation due to radiative heat transfer is an order of magnitude less than those due to conduction and convection. This is very clear from Figure 5-28 which compares the conductive and radiative fluxes at the combustor and nozzle wall. Figures 5-29 and 5-30 show the radiative fluxes in the axial and radial directions. It is observed that heat is transferred from the combustion chamber to the nozzle region by radiation. The predicted ISP for this case is about 314 which is very close the TRW's experimental data of 310. The ISP predicted in this case is significantly less than the ISPs predicted without the inclusion of radiation model. This is because a constant temperature boundary condition is used for all the radiation cases whereas a zero gradient boundary condition is used for all the cases with no radiation. The conductive and radiative heat loss at the walls leads to a lower ISP.
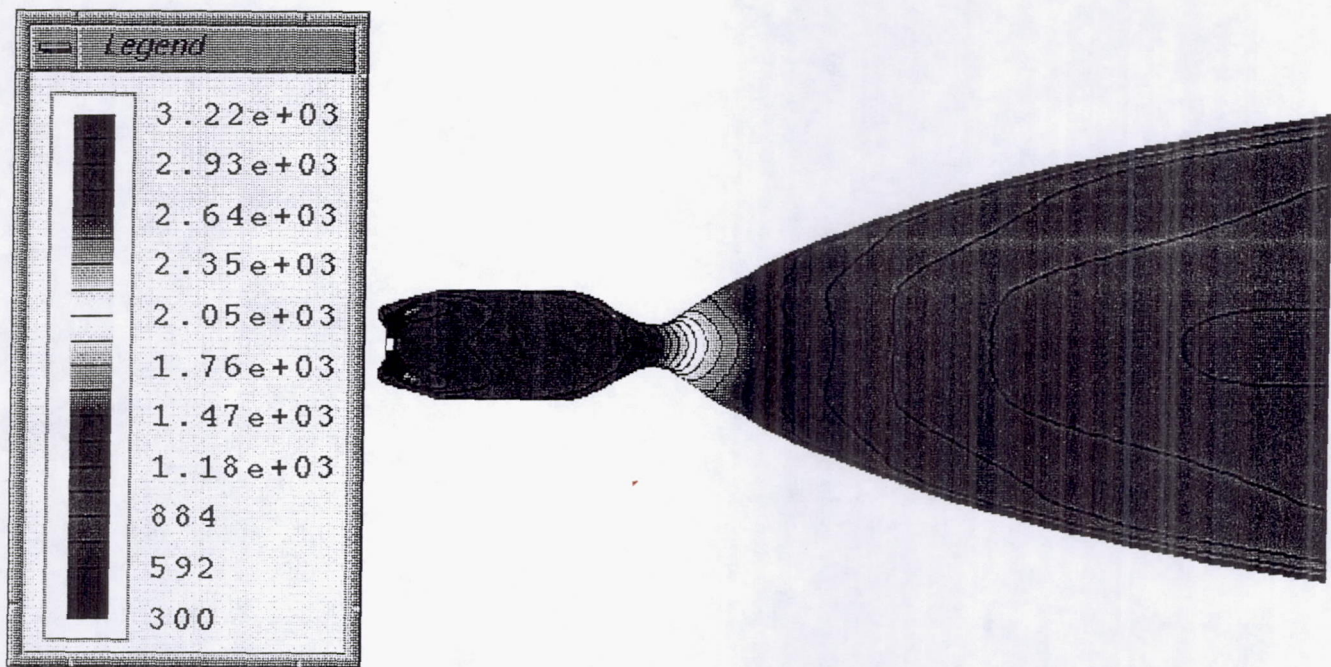


Figure 5-26. Temperature Distribution (Gas-Gas Model, 100% Power Level with Radiation)

4075/3

Legend

3.18e+03
2.89e+03
2.6e+03
2.32e+03
2.03e+03
1.74e+03
1.45e+03
1.16e+03
876
588
300
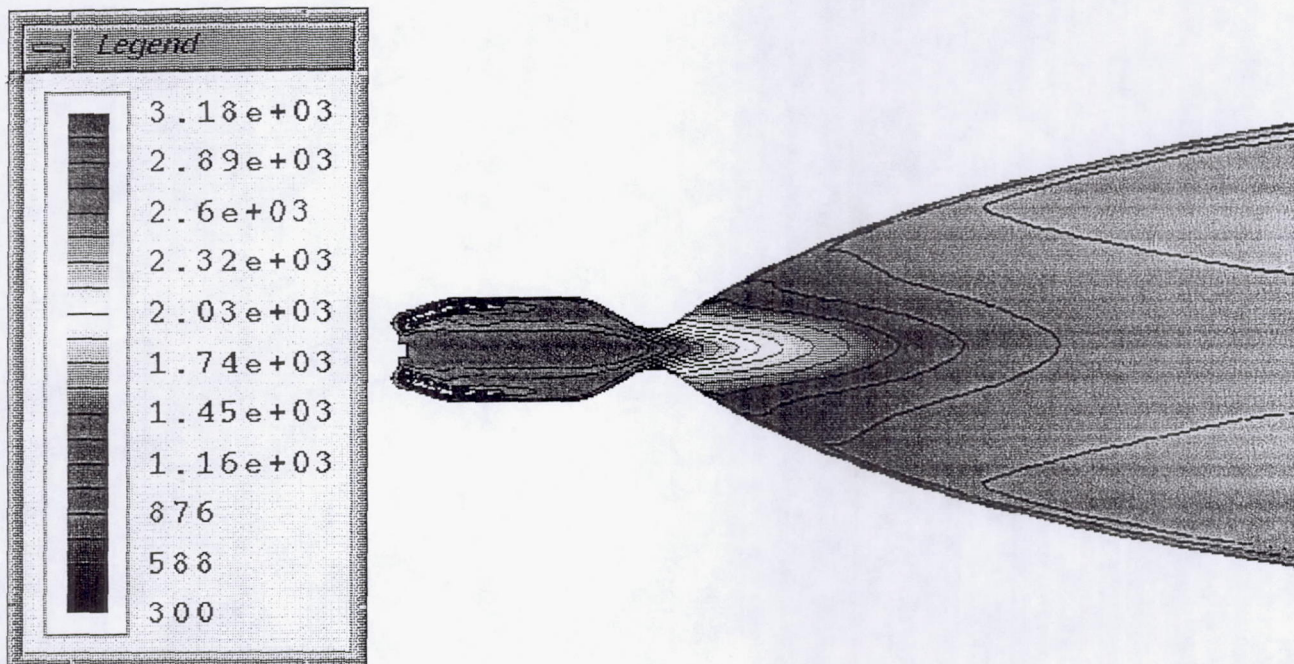
Figure 5-27. Temperature Distribution (Spray Model, 100% Power Level with Radiation)
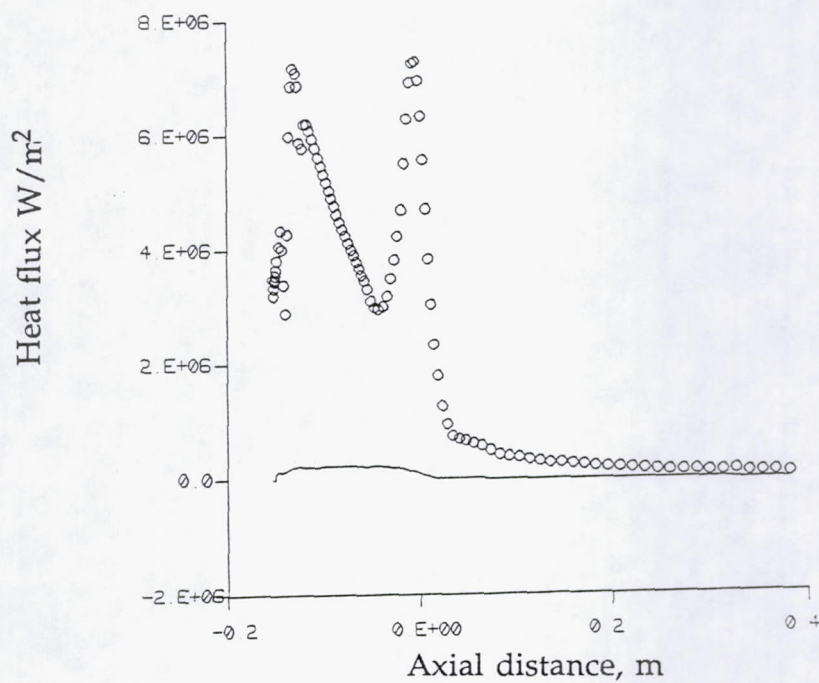


Figure 5-28. Comparison of Conductive and Radiative Fluxes at Nozzle Wall; o, - conductive heat flux; ---, radiative heat flux (Gas-Gas Mode, 100% Power Level)

62
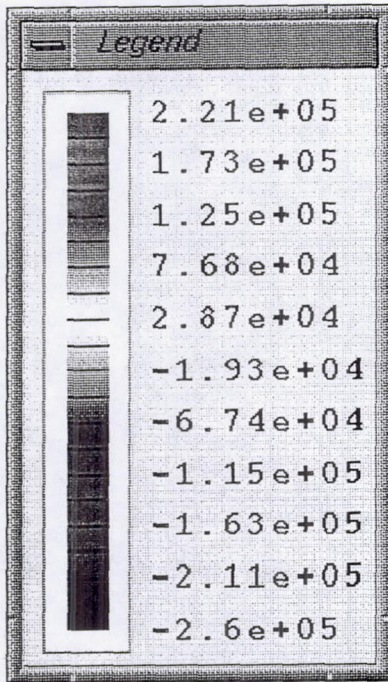
Figure 5-29. Distribution of Axial Radiation Flux (Gas-Gas Model, 100% Power Level)

Legend
2.21e+05
1.73e+05
1.25e+05
7.68e+04
2.87e+04
-1.93e+04
-6.74e+04
-1.15e+05
-1.63e+05
-2.11e+05
-2.6e+05
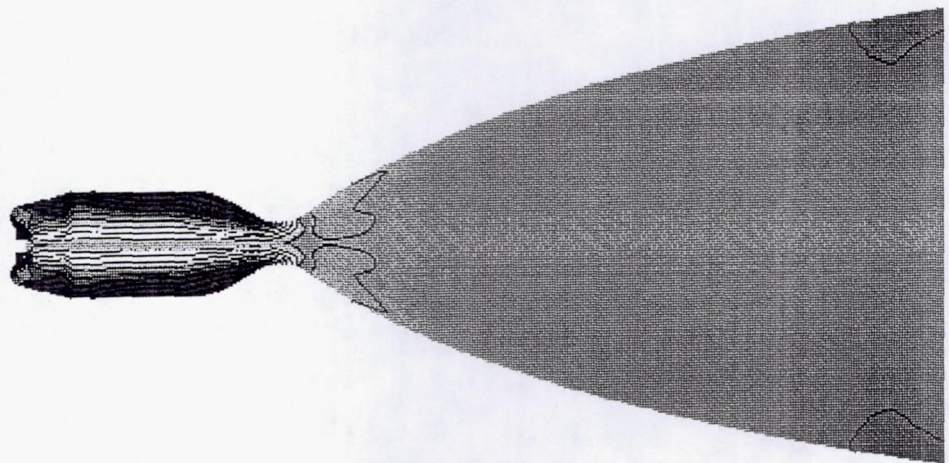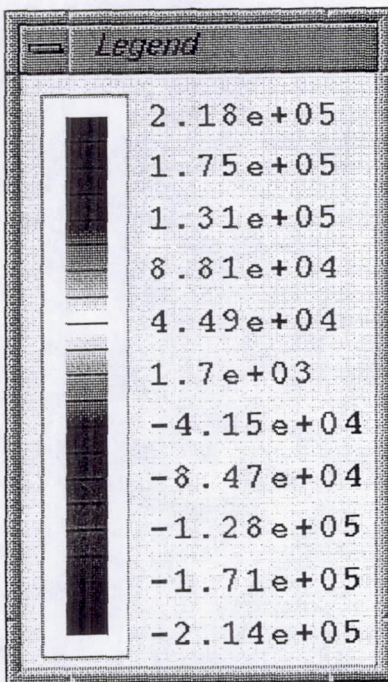


Figure 5-30. Distribution of Radial Radiative Flux (Gas-Gas Model, 100% Power Level)

Legend
2.18e+05
1.75e+05
1.31e+05
8.81e+04
4.49e+04
1.7e+03
-4.15e+04
-8.47e+04
-1.28e+05
-1.71e+05
-2.14e+05

63

4075/3

## 5.4    Heat Shield Analysis

The heat shield on VTE has been designed to minimize the radiative heat loss from the engine.  The amount of radiative heat loss from the chamber and nozzle walls depend on wall temperature and their radiative properties.  In order to understand the effects of heat shield on flow patterns and radiative heat transfer characteristics, simulations were performed with and without the inclusion of the radiation model.

Figure 2-3 showed the 120 X 40 computational grid used for this problem.  The dimensions for the heat shield were obtained from technical drawings supplied by TRW.  The grid for VTE is embedded within the grid for shield.  The computational domain was extended beyond the nozzle exit in order to resolve the expansion of nozzle flow into the vacuum environment.  Simulations were performed for 100% power level with gas-gas combustion model and laminar flow conditions.  These assumptions are justified since the inclusion of spray dynamics and turbulence is not expected to play a role in the heat shield.

First the flow characteristics inside the heat shield is studied without invoking the radiation model.  Figure 5-31 shows the Mach number contours for this case.  The contours inside the combustor and nozzle are very similar to those obtained from the calculations without the heat shield.  However, the expansion of the gas into the heat shield after it leaves the nozzle is observed by the curving of the contour lines.  The amount of flow entrained into the heat shield is estimated to be negligibly small.  Figure 5-32 shows the temperature distribution for this case. For one-to-one comparison with the radiation results, a constant temperature boundary condition is applied for obtaining this figure.  A temperature of 1000°K is imposed at the chamber/nozzle walls and a temperature of 300°K is imposed at the shield walls.  Due to this reason, the temperature of the fluid inside the shield region is relatively cold, but its density is of the order of 1.0E-05 $kg/m^3$.  Since the density of the fluid in the shield is extremely small, its influence on flow and heat transfer processes are expected to be negligible.

4075/3

```
MACH  CONTOURS
FMIN  2.140E-08
FMAX  4.817E+00
CONTOUR LEVELS
  2   1.661E-01
  4   4.983E-01
  6   8.305E-01
  8   1.163E+00
 10   1.495E+00
 12   1.827E+00
 14   2.159E+00
 16   2.492E+00
 18   2.824E+00
 20   3.156E+00
 22   3.488E+00
 24   3.821E+00
 26   4.153E+00
 28   4.485E+00
 30   4.817E+00
```

Figure 5-31.  Mach Number Distribution in VTE (Gas-Gas Model, 100% Power Level, No Radiation)



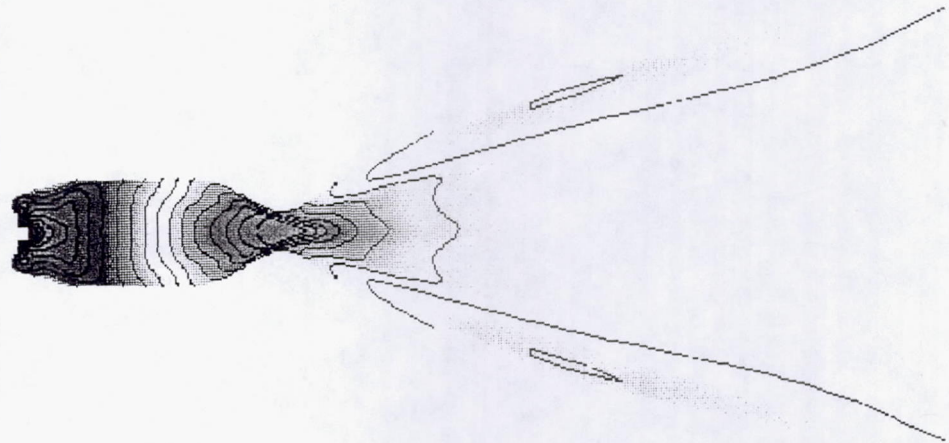Figure 5-32.  Temperature Distribution (Gas-Gas Model, 100% Power Level, No Radiation)

4075/3

For the same problem, the radiative heat transfer characteristics in the shield is studied by invoking the radiation model. Since the wall temperature distributions are not known, the combustor and nozzle walls are assumed to be maintained at 1000°K and the shield walls are maintained at 300°K. Figures 5-33 and 5-34 show the Mach number and temperature contours for this case. The distributions of Mach number and temperature in the chamber and nozzle are very similar to the results of the previous case. However, from the Mach number contours, it is observed that more fluid is entrained into the shield when radiation effects are included. The temperature contours indicate that the plume is relatively cold when compared with the predictions without the radiation model. Thus the energy lost due to radiation results in a colder plume. Figures 5-35 and 5-36 show contours of radiative fluxes in the axial and radial directions. The heat radiated by nozzle wall into the shield region can be clearly seen. It can also be seen that heat is being radiated away from the combustor region into the nozzle. Since the radiative heat flux at the exit is positive, some amount of heat from the nozzle region is lost by way of radiation.

Figures 5-37 and 5-38 compare the conductive and radiative heat fluxes at the nozzle and outer shield walls. At the nozzle wall, the convective heat fluxes are much higher than the radiative heat flux. On an average, the radiative heat transfer is found to be less than 8% of the conductive heat transfer. On the other hand, the radiative heat flux at the outer shield wall is much higher than the conductive heat flux, but small when compared with the heat flux at the nozzle wall. Thus small amount of heat is lost from the shield to outer space due to radiation.

```
MACH   CONTOURS
FMIN   5.436E-08
FMAX   4.860E+00
CONTOUR LEVELS
  2    1.676E-01
  4    5.028E-01
  6    8.380E-01
  8    1.173E+00
 10    1.508E+00
 12    1.844E+00
 14    2.179E+00
 16    2.514E+00
 18    2.849E+00
 20    3.184E+00
 22    3.520E+00
 24    3.855E+00
 26    4.190E+00
 28    4.525E+00
 30    4.860E+00
```
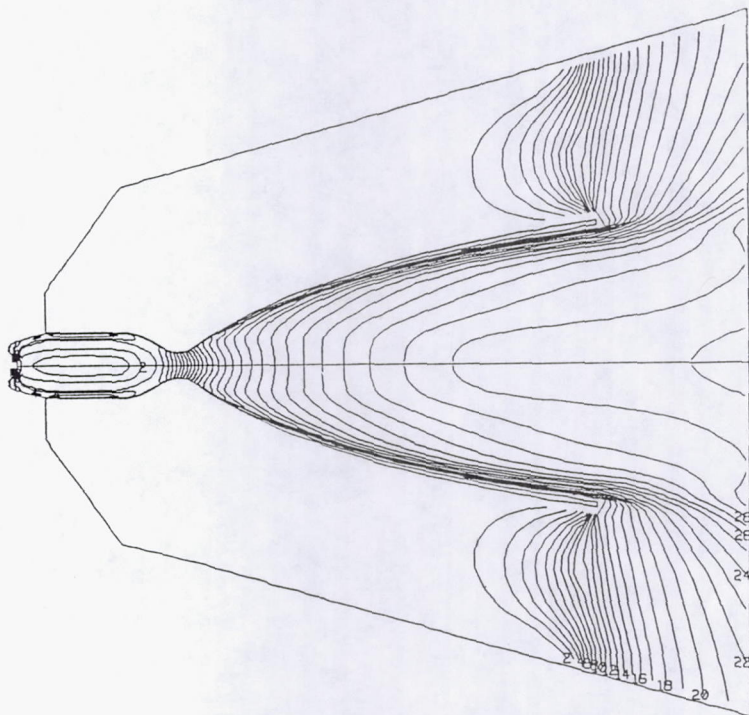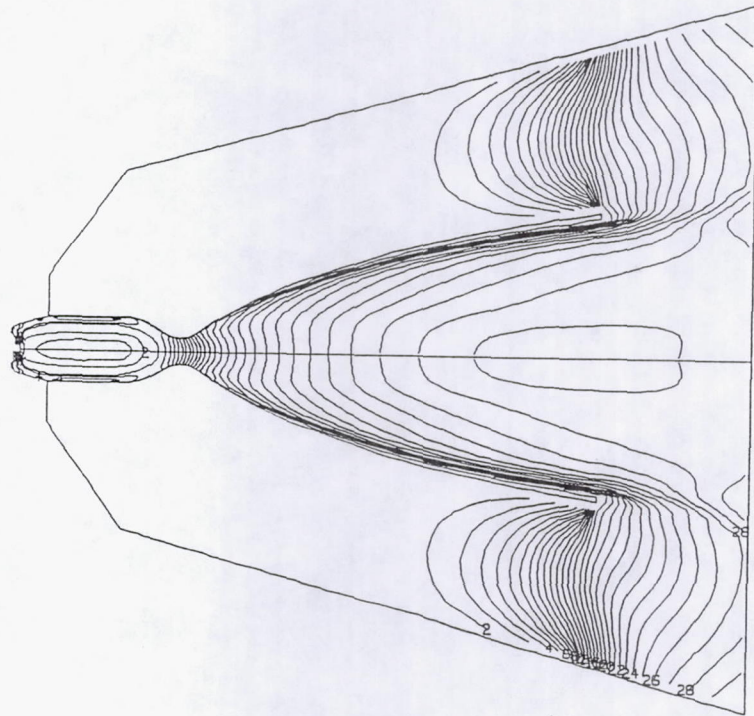
Figure 5-33.  Mach Number Distribution in VTE (Gas-Gas Model, 100% Power Level, with Radiation)
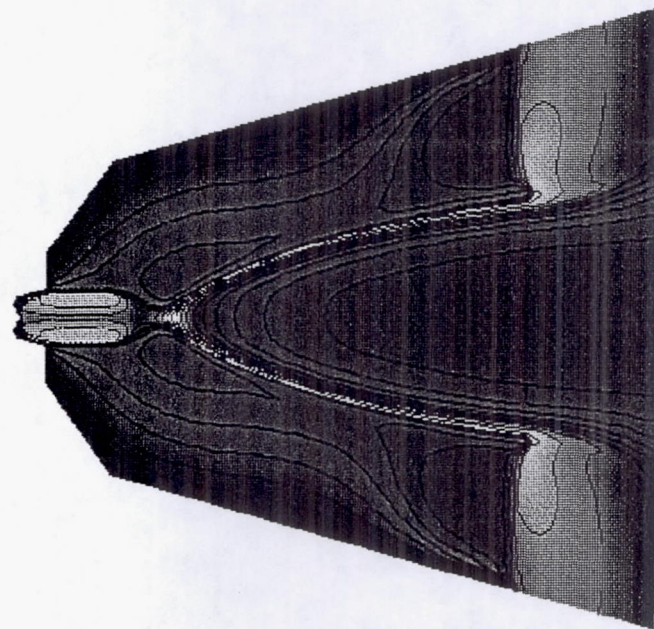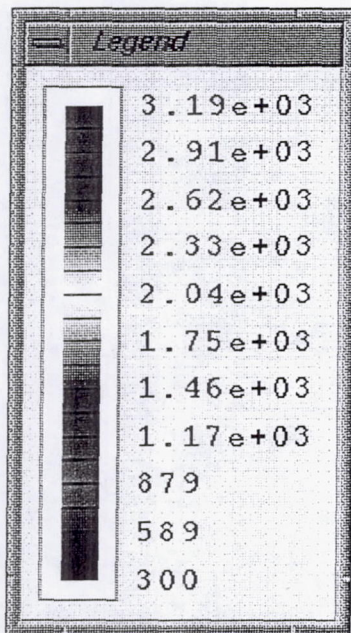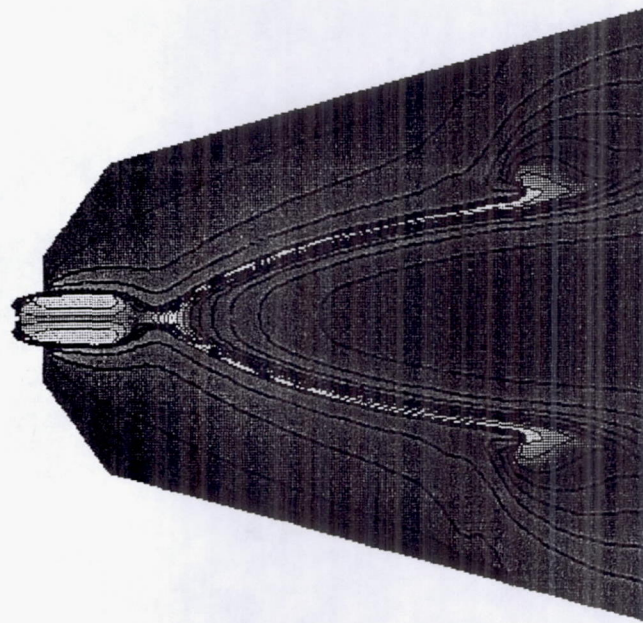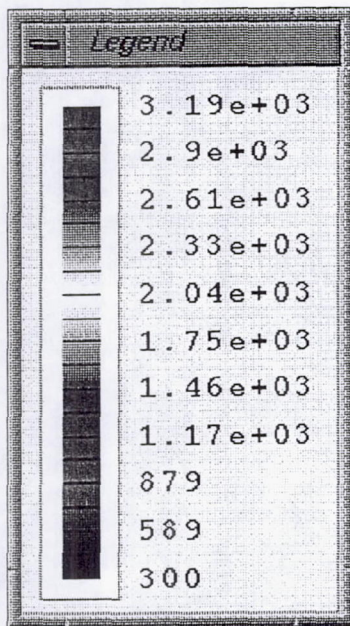


Figure 5-34.  Temperature Distribution (Gas-Gas Model, 100% Power Level, with Radiation)

4075/3
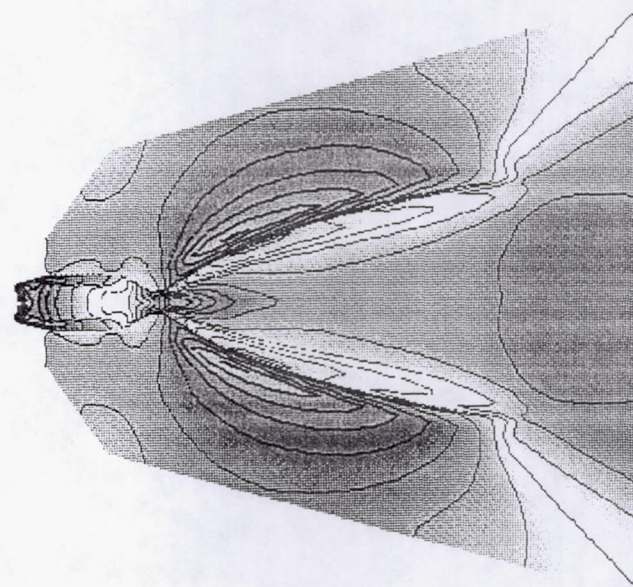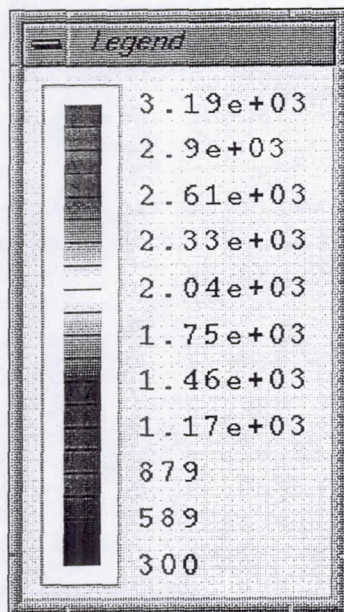
Figure 5-35. Distribution of Axial Radiative Flux (Gas-Gas Model, 100% Power Level)
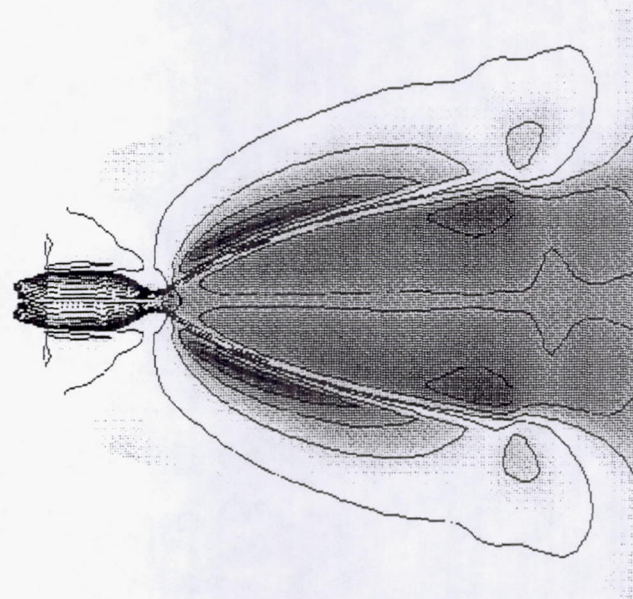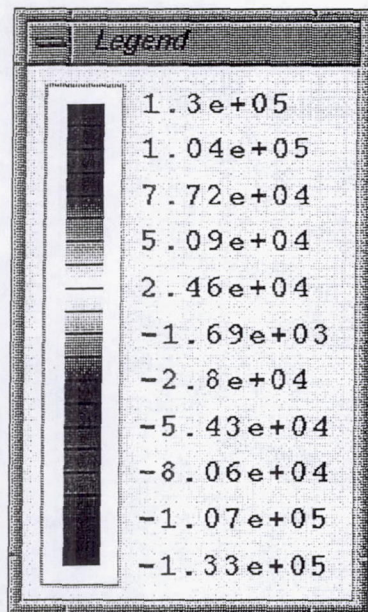


Figure 5-36. Distribution of Radial Radiative Heat Flux (Gas-Gas Model, 100% Power Level)

68

4075/3
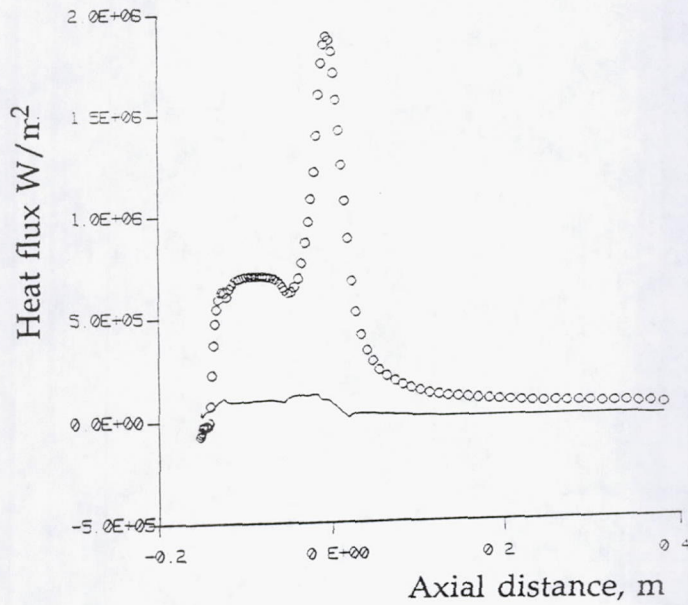
Figure 5-37. Comparison of Conductive and Radiative Fluxes at Nozzle Wall; o, - conductive flux; ---, radiative flux (Gas-Gas Model, 100% Power Level)
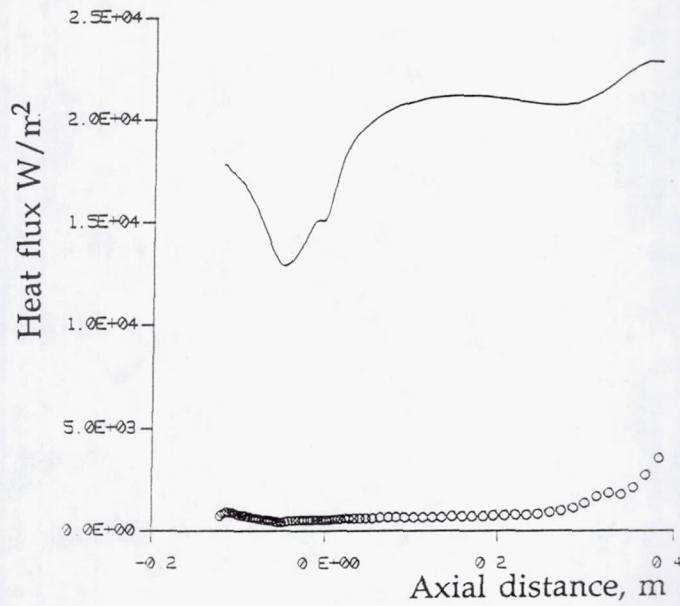


Figure 5-38. Comparison of Conductive and Radiative Fluxes at Shield Wall; o, - conductive flux; ---, radiative flux (Gas-Gas Model, 100% Power Level)

69

# 6. CONCLUSIONS AND RECOMMENDATIONS

## 6.1 Accomplishments

a. A two-liquid, two-phase Eulerian-Lagrangian spray model has been incorporated into the REFLEQS code.

b. The spray tracking methodology has been extended to account for complex, non-orthogonal BFC grids and interaction of the spray with the domain boundaries.

c. A complete coupling between the gas phase and the liquid droplets has been implemented through source/sink terms for the mass, momentum, and energy equations of both phases.

d. A chemical equilibrium model (based on the element potential method) has been incorporated into the code. This model has been validated against the predictions of the TDK code.

e. A linear stability analysis model has been included to estimate drop sizes resulting from the impingement of two axisymmetric liquid sheets.

f. A stochastic droplet dispersion model has been implemented into the code to model the droplet-turbulence interaction.

g. A hot gas radiation model (based on the discrete ordinate approach) has been incorporated into the code. The model has been validated for simple problems having exact solutions.

The above capabilities in conjunction with the existing capabilities of REFLEQS have facilitated the simulation of complex physical phenomenon in liquid rocket engines such as OMV/VTE combustors. However, certain limitations and shortcomings do exist that need to be addressed in the future.

## 6.2    Summary of Findings from the Numerical Analysis

A number of simulations were obtained to analyze the performance of VTE at different power levels. Predictions using the gas-gas and the liquid-gas spray models have been compared. In most of the cases (both gas-gas and spray models), the predicted ISP is approximately 320 which is slightly higher than the measured value of 310. The ISP is overpredicted because the heat loss from the engine walls is not included in our study when adiabatic boundary conditions are imposed at the walls. In general, the gas-gas model predicts a higher ISP than that predicted by the spray model, because the energy required to atomize and evaporate the droplets are not present in the gas-gas model. For both the models, the predicted ISP slightly decreases at off-design power levels indicating a decrease in efficiency.

The predictions of spray model suggest that smaller droplets evaporate faster, leading to better mixing in the combustion chamber. This results in better performance of the engine. The larger droplets, on the other hand, are shown to impinge on the splash plate providing a cooling effect for the wall. It is shown that optimum performance can be achieved when the droplet sizes are in the 25-50 microns range. The predictions of gas-gas model show two recirculation zones: one in the swept bach region of the combustor and the other in the center of the chamber. These recirculation zones are absent in the predictions of the spray model. The recirculating zones in the predictions of gas-gas model are mainly induced by the relatively high inlet velocity of the gases. The predictions also show that the hottest region is at the center of the combustion chamber. As a result, the head end of the pintle injector is expected to be very hot. This has been observed in VTE hot fire tests. Later designs of the VTE engine has an ablative material covering the head end.

Predictions using the radiation model suggest that radiation effects on flow and heat transfer inside the VTE combustion chamber and nozzle are insignificant. The radiative heat flux at the walls are an order of magnitude less than the conductive heat flux. The results show that heat is transferred from the combustion chamber zone to the nozzle region by radiation. Simulations performed with the heat shield show that negligible amount of fluid is entrained into the heat shield region. However, the heat shield is shown to be effective in protecting the OMV structure

71

around the engine from the radiated heat. Due to the limitted knowledge of the radiative properties of the OMV combustion gases, very high values of gas absorptivity and wall emissivity are used. For more realistic values of radiative properties, the contribution due to radiative heat transfer is expected to be smaller.

### 6.3    Suggestions for Future Work

a.    An advanced model for atomization due to impingement of unlike liquids in sheet (2-D) and round jets (3-D) forms. In the present analysis, a simplified surface wave model was used to estimate the mean droplet size. This surface wave model considers the instability of waves on like impinging jets in a stagnant environment. On the other hand, in the VTE engine, unlike jets impinge in a reacting gas environment. Hence the present simplified atomization model overpredicts the droplet size. A rigorous model including the effects of ambient reacting gas is needed in order to accurately predict the droplet size.

b.    The development of a coupled atomization model. In the actual conditions inside the VTE engine, the droplet sizes are expected to be a strong fuction of local gas conditions. The relative velocity between the liquid sheet and the gas will vary along the sheet radius resulting in droplet size variation. The simplified atomization model, on the other hand, only predicts a single mean size based on the most unstable wavelength. Thus, a technique such as the Jet-Embedding technique[23,] needs to be developed for atomization in impinging jets.

c.    Development of advanced models to simulate mixing and combustion in the liquid phase. When unlike jets impinge on each other, the resulting droplets are inhomogeneous. In order to predict the composition of droplets, the mixing occuring in the liquid phase needs to be modeled. This requires a solution of the liquid phase equations near the impingement point. Since the liquid phase equations near the impingement point are strongly elliptic and since free surfaces are involved, obtaining a solution for this problem would represent a major effort.

72

d.  Identification and implementation of reduced finite rate reaction mechanisms for complex fuel/oxidizer combinations. In the calculations of the present study, an equilibrium chemistry model was used to simulate combustion. For steady state calculations, this model was shown to provide satisfactory results. However, for studying transient phenomena such as combustion instabilities, a finite rate reaction models are necessary. For the reaction between MMH and NTO, several reaction steps with 200 species are involved. A detailed modeling of this reaction would be prohibitively expensive. Hence reduced finite rate reaction models need to be developed for MMH-NTO and other commonly used propellants such as H2-O2.

e.  Implementation of dense spray models to simulate the spray in the region close to the injector. The present spray model assumes that the volume occupied by the droplets are small when compared to the cell volume. This assumption does not hold good near the injector where the spray is dense. The dense spray effects are thus need to be included in the calculation procedure.

f.  Development and incorporation of models to account for supercritical behavior of fluids. Engines such as SSME operate under supercritical pressure conditions. The effects of supercritical conditions on evaporation and heat transfer are shown to be important due to the abrupt changes in fluid properties. Several models are available for supercritical vaporization and heat transfer. These models should be incorporated in the present code.

g.  Extend the droplet dispersion model to non-isotropic turbulence. The turbulent droplet dispersion model currently implemented in the code assumes that turbulence is locally isotropic. This assumption is strictly not valid in the VTE combustion chamber. For accurate prediction of droplet dispersion, the effect of non-isotropy must be considered.

# 7. REFERENCES

1.  Krishnan, A., and Przekwas, A.J., "Orbital Maneuvering Vehicle (OMV): Thrust Chamber Performance," Interim Report for Phase I, Contract Number: NAS8-37196, CFDRC Report 4075/1, July 1990.

2.  Krishnan, A., and Przekwas, A.J., "Orbital Maneuvering Vehicle (OMV): Thrust Chamber Performance," Contract Number: NAS8-37196, CFDRC Report 4075/2, September 1991.

3.  A. Krishnan, A.J. Przekwas, and K.W. Gross, "Spray Combustion in Liquid Rocket Engine Thrust Chambers," 28th JANNAF Combustion Meeting, October 1991.

4.  A. Krishnan, A.J. Przekwas, and K.W. Gross, "Computational Analysis of Liquid Hypergolic Propellant Rocket Engines," AIAA-92-1552, March 1992.

5.  Peric, M., Kessler, R., and Scheuerer, G., "Comparison of Finite-Volume Numerical Methods with Staggered and Colocated Grids," *Computers and Fluids*, vol. 16, no. 4, pp. 389-403, 1988.

6.  Przekwas, A.J., Habchi, S.D., Yang, H.Q., Avva, R.K., Talpallikar, M.V., and Krishnan, A., "REFLEQS-2D: A Computer Program for Turbulent Flows with and without Chemical Reaction, Volume 1: User's Manual," CFDRC Report GR-88-4, 1990.

7.  Meintjes, K., and Morgan, A.P., "Element Variables and the Solution of Complex Chemical Equilibrium," *Comb. Sci. Tech,*, vol. 68, pp. 35-48, 1989.

8.  Viskanta, R., and Menguc, M.P., "Radiation Heat Transfer in Combustion Systems," *Prog. Energy Combustion Sci.*, vol. 13, pp. 97-160, 1987.

9.  Howell, J.R., "Thermal Radiation in Participating Media: The Past, the Present, and Some Possible Futures," *Trans. ASME*, vol. 110, pp. 1220-1229, November 1988.

10. Hottel, H.C., and Sarofin, A., Radiative Transfer, McGraw-Hill, New York, 1967.

11. Truelove, J.S., "Evaluation of a Multi-Flux Model for Radiative Heat Transfer in Cylindrical Furnaces," AERE Report, May 1978.

12. Bayazitoglu, Y., and Higenyi, J., "Higher Order Differential Equations of Radiative Transfer: $P_3$ Approximation," *AIAA Journal*, vol. 17, no. 4, pp. 424-431, 1979.

4075/3

13. Siegel, R., and Howell, J.R., <u>Thermal Radiation Heat Transfer</u>, McGraw-Hill, 1981.

14. Lockwood, F.C., and Shah, N.G., "A New Radiation Solution Method for Incorporation in General Combustion Prediction Procedures," *8th Symposium (International) on Combustion*, 1981.

15. Fireland, W.A., "Discrete-Ordinates Solutions of the Radiative Transport Equation for Rectangular Enclosures," *J. Heat Transfer*, vol. 106, pp. 699-706, 1984.

16. Fireland, W.A., and Jamaluddin, A.S., "Three-Dimensional Spectral Radiative Heat Transfer Solutions by the Discrete-Ordinates Method," *J. Thermophysics*, vol. 5, no. 3, pp. 335-339, 1991.

17. Truelove, J.S., "Discrete-Ordinate Solutions of the Radiation Transport Equation," *Trans. ASME*, vol. 109, pp. 1048-1051, 1987.

18. Jendoubi, S., and Lee, H.S., "Comparisons of Cylindrical and Rectangular Media Radiative Transfer Solutions Using the S-N Discrete Ordinates Method," AIAA-92-2894, 1992.

19. Crowe, C.T., Sharma, M.P., and Stock, D.E., "The Particle-Source-in-Cell (PSI-CELL) Model for Gas-Droplet Flows," *J. Fluids Eng.*, pp. 325-332, 1977.

20. Gosman, A.D., and Ioannides, E., "Aspects of Computer Simulation of Liquid-Fueled Combustors," AIAA-81-0323, 1981.

21. Weihs, D., "Stability of Thin, Radially Moving Liquid Sheets," *J. Fluid Mech.*, vol. 87, pp. 289-298, 1978.

22. Nickerson, G.R., Coats, D.E., Dang, A.L., Dunn, S.S., and Kehtarnavag, H., "Two-Dimensional Kinetics (TDK) Nozzle Performance Computer Program, Volume 2: Programming Manual," NAS8-36863, March 1989.

23. Giridharan, M.G., Lee, J.G., Krishnan, A., Przekwas, A.J., and Gross, K., "A Numerical Model for Coupling Between Atomization and Spray Dynamics in Liquid Rocket Thrust Chambers," AIAA-92-3769, 1992.

4075/3

# APPENDIX A

## SAMPLE INPUT FILES

# Appendix A

## Sample Input Files

```
auto2d
* Input data for the OMV Variable Thrust Engine
***************Gas-Gas Model****************************
title OMV-VTE (100x30,modvil=3,turbulent,MMH/N2O4)
*-------------------- Parameters --------------------*
* ox stands for oxidizer, fu stands for fuel.
integer L=100
integer M=30
real uox=110.52  vox=-51.53
real ufu=0.0  vfu=144.3
real Tinlet=300.0  Pinlet=6.89250E+05
*-------------------- Geometry & Grid -------------------*
l L  ; m M
polar T ; bfc T ; orthog F
*

grid from omvGRID
*-------------------- Solution control -----------------*
niter 1000 ; info 0
algorithm simplec ; scheme upwind all
*

solve nvu nvv nvpp nvk1 nvd1 nvh
*

absor 1.0; scatr 0.0; emisw 1.0
*

niterp 5 ; iblox nvpp 0 ; ibloy nvpp 0
*

nsweep nvu 10 ; nsweep nvv 10 ; nsweep nvpp 30 ; nsweep nvk1 10
nsweep nvd1 10 ; nsweep nvh 10 ; nsweep nvf1 10 ; nsweep nvf2 10
*

dtfals nvu 1.5 ; dtfals nvv 1.5 ; dtfals nvk1 1.5 ; dtfals nvd1 1.5
dtfals nvh 1.5 ; dtfals nvf1 1.5 ; dtfals nvf2 1.5
*

relax nat 0.2 ; relax narho 0.2 ; relax nap 0.2 ;relax navis 0.2
fimax navis 0.1
*---------------- Output Control ------------------*
Iprint nvu 0 ; Iprint nvv 0 ; Iprint nap 0
cuser T ; pltdmp t ; Idump 50
i1dbg 50 ; ildbg 56 ; j1dbg 25 ; jldbg 30
*------------ Physical properties and models -------------*
press 0.E+05 ;  moden 3 ;  comprs T ; mixing 2 ; modvds 0
modvis 2  ; modwal 3 ; modvil 3 ; ICP 3 ; iequil 1 ; modken 1
*-------------------------------------------------------*
ncmps 2
compos 1 n2o4 1.0 h 0.0 h2 0.0 h2o 0.0 no 0.0 co 0.0 ch4 0.0
compos 2 ch6n2 1.0 n2 0.0 o 0.0 oh 0.0 o2 0.0 co2 0.0
*---------------- Initial Conditions -------------------*
```

```
uin 100. ; vin 50. ; presin Pinlet ; temin 2000. ; compin 7
*restart from MODEL.AUR
*---------------- Boundary region setup --------------------*
nblock 1
poros vol 0.0  1  7  1  5
*--------------------------------------------------------*
nreg 9
region 1  west   fixm    1   1   6    9
region 2  west   wall    1   1   10   30
region 3  west   wall    8   8   1    5
region 4  east   extrap  L   L   1    M
region 5  south  symm    8   L   1    1
region 6  south  wall    1   1   6    6
region 7  south  fixm    2   4   6    6
region 8  south  wall    5   7   6    6
region 9  north  wall    1   L   M    M
*----------- Boundary Condtion Specifications --------------*
uvela uox ; vvela vox ; presa Pinlet ; tema Tinlet ; compa 1
uvelb ufu ; vvelb vfu ; presb Pinlet ; temb Tinlet ; compb 2
bc vu = va
bc set 1 vu
bc vu = vb
bc set 7 vu
bc vu = 0.0
bc vu nvh = zgbc
bc set 2  vu
bc set 3  vu
bc set 4  vu
bc set 5  vu
bc set 6  vu
bc set 8  vu
bc set 9  vu
end
```

```
auto2d
* Input data for the OMV Variable Thrust Engine
*************Spray Model*************************
title OMV-VTE (100x30,modvil=3,turbulent,MMH/N2O4)
*-------------------- Parameters --------------------*
* ox stands for oxidizer, fu stands for fuel.
integer L=100
integer M=30
real Tinlet=300.0  Pinlet=6.89250E+05
*-------------------- Geometry & Grid -------------------*
l L ; m M
polar T ; bfc T ; orthog F
*
grid from omvGRID unform
*------------------- Solution control -----------------*
niter 1000 ; info 0
algorithm simplec ; scheme upwind all
*
solve nvu nvv nvpp nvk1 nvd1 nvh
*
niterp 5 ; iblox nvpp 0 ; ibloy nvpp 0
*
nsweep nvu 10 ; nsweep nvv 10 ; nsweep nvpp 30 ; nsweep nvk1 10
nsweep nvd1 10 ; nsweep nvh 10 ; nsweep nvf1 10 ; nsweep nvf2 10
*
dtfals nvu 1.0 ; dtfals nvv 1.0 ; dtfals nvk1 1.0 ; dtfals nvd1 1.0
dtfals nvh 1.0 ; dtfals nvf1 1.0 ; dtfals nvf2 1.0
*
relax nat 0.3 ; relax narho 0.3 ; relax nap 0.3
*---------------- Output Control -----------------*
cuser T ; pltdmp t ; Idump 50
Iprint nvu 0 ; Iprint nvv 0 ; Iprint nap 0
*------------ Physical properties and models -------------*
press 0.E+05 ;  moden 3 ;  comprs T ; mixing 2 ; modvds 0
modvis 2  ; modwal 3 ; modvil 3 ; ICP 3 ; iequil 1; modken 1
*---------------------------------------------------------*
ncmps 2
compos 1 n2o4 1.0 h 0.0 h2 0.0 h2o 0.0 no 0.0 co 0.0 ch4 0.0
compos 2 ch6n2 1.0 n2 0.0 o 0.0 oh 0.0 o2 0.0 co2 0.0
*---------------- Initial Conditions ------------------*
uin 100. ; vin 50. ; presin Pinlet ; temin 3000. ; compin 7
*restart from MODEL.AUR
*---------------- Spray data ----------------------*
spray t
tboil1  300. ; cpl1 1580.0 ; hll1 414000.0 ; rhol1 1433.0
psatl1 1.2E5
```

```
tboil2  360. ; cpl2 3000.0 ; hll2 875000.0 ; rhol2 870.0
psatl2 6.7E3
iuser 52 1 ; iuser 53 5
nslot 2
*------------- slot 1 -------------------------*
inject slot 1  20  1  0.1460  CELL 4  7
inject size 1  lognormal  50.0e-6  25.0e-6  100.0e-6  0.2
inject bc   1  25.0  27.0  0.0  300.0
*------------- slot 2 -------------------------*
inject slot 2  20  2  0.0890  CELL 4  7
inject size 2  lognormal  50.0e-6  25.0e-6  100.0e-6  0.2
inject bc   2  25.0  23.0  0.0  300.0
*---------------- Boundary region setup --------------------*
nblock 1
poros vol 0.0  1  7  1  5
*----------------------------------------------------*
nreg 10
region 1  west   wall    1   1   1    5
region 2  west   fixm    1   1   6    9
region 3  west   wall    1   1  10   30
region 4  west   wall    8   8   1    5
region 5  east   extrap  L   L   1    M
region 6  south  symm    1   L   1    1
region 7  south  wall    1   1   6    6
region 8  south  fixm    2   4   6    6
region 9  south  wall    5   7   6    6
region 10 north  wall    1   L   M    M
*---------- Boundary Condtion Specifications --------------*
uvela 0.0 ; vvela 0.0 ; presa Pinlet ; tema Tinlet ; compa 1
uvelb 0.0 ; vvelb 0.0 ; presb Pinlet ; temb Tinlet ; compb 2
bc vu = va
bc set 2 vu
bc vu = vb
bc set 8 vu
bc vu = 0.0
bc set 5 vu
bc vu = 0.0
bc vu nvh = zgbc
bc set 1 vu
bc set 3  vu
bc set 4  vu
bc set 6  vu
bc set 7 vu
bc set 9 vu
bc set 10 vu
end
```

| 4. Title and Subtitle | | 5. Report Date |
|---|---|---|
| Computational Analysis of Variable Thrust Engine (VTE) Performance | | February 1993 |
| | | 6. Performing Organization Code |

| 7. Author(s) | | 8. Performing Organization Report No. |
|---|---|---|
| M.G. Giridharan, A. Krishnan, A.J. Przekwas | | 4075/3 |
| | | 10. Work Unit No. |

| 9. Performing Organization Name and Address | | 11. Contract or Grant No. |
|---|---|---|
| CFD Research Corporation 3325 Triana Blvd. Huntsville, AL 35805 | | NAS8-37196 |
| | | 13. Type of Report and Period Covered |
| 12. Sponsoring Agency Name and Address | | April 21, 1989–Jan. 93 Final Report |
| National Aeronautic and Space Administration George C. Marshall Space Flight Center Alabama 35812 | | 14. Sponsoring Agency Code |

15. Supplementary Notes

16. Abstract

The Variable Thrust Engine (VTE) of the Orbital Maneuvering Vehicle (OMV) uses a hypergolic propellant combination of Monomethyl Hydrazine (MMH) and Nitrogen Tetroxide (NTO) as fuel and oxidizer, respectively. The performance of the VTE depends on a number of complex interacting phenomena such as atomization, spray dynamics, vaporization, turbulent mixing, convective/radiative heat transfer, and hypergolic combustion.

This study involved the development of a comprehensive numerical methodology to facilitate detailed analysis of the VTE. An existing Computational Fluid Dynamics (CFD) code was extensively modified to include the following models: (i) a two-liquid, two-phase Eulerian-Lagrangian spray model; (ii) a chemical equilibrium model; and (iii) a discrete ordinate radiation heat transfer model. The modified code was used to conduct a series of simulations to assess the effects of various physical phenomena and boundary conditions on the VTE performance. The details of the models and the results of the simulations are presented in this report.

| 17. Key Words (Suggested by Author(s)) | 18. Distribution Statement | | |
|---|---|---|---|
| Variable Thrust Engine (VTE), impinging jets, liquid spray, equilibrium chemistry, radiative heat transfer | | | |
| 19. Security Classif. (of this report) | 20. Security Classif. (of this page) | 21. No. of pages | 22. Price |
| | | 90 | |